RESEARCH ARTICLE

# Morphological properties of the axon initial segment-like process of AII amacrine cells in the rat retina

Jian Hao Liu ⓘ | Jeet Bahadur Singh ⓘ | Margaret Lin Veruki ⓘ | Espen Hartveit ⓘ

Department of Biomedicine, University of Bergen, Bergen, Norway

**Correspondence**
Espen Hartveit, Department of Biomedicine, University of Bergen, Jonas Lies vei 91, N-5009 Bergen, Norway.
Email: espen.hartveit@uib.no

## Abstract

Signal processing within the retina is generally mediated by graded potentials, whereas output is conveyed by action potentials transmitted along optic nerve axons. Among retinal neurons, amacrine cells seem to be an exception to this general rule, as several types generate voltage-gated $Na^+$ ($Na_v$) channel-dependent action potentials. The AII, a narrow-field, bistratified axon-less amacrine cell found in mammalian retinas, displays a unique process that resembles an axon initial segment (AIS), with expression of $Na_v$ channels colocalized with the cytoskeletal protein ankyrin-G, and generates action potentials. As the role of spiking in AIIs is uncertain, we hypothesized that the morphological properties of the AIS-like process could provide information relevant for its functional importance, including potential pre- and/or postsynaptic connectivity. For morphological analysis, we injected AII amacrine cells in slices with fluorescent dye and immunolabeled the slices for ankyrin-G. Subsequently, this enabled us to reliably identify AII-type processes among ankyrin-G-labeled processes in wholemount retina. We systematically analyzed the laminar localization, spatial orientation, and distribution of the AIS-like processes as a function of retinal eccentricity. In the horizontal plane, the processes displayed no preferred orientation and terminal endings were randomly distributed. In the vertical plane, the processes displayed a horizontal preference, but also ascended and descended into the inner nuclear layer and proximal inner plexiform layer, respectively. These results suggest that the AII amacrine AIS-like process is unlikely to take part in conventional synaptic connections, but may instead be adapted to respond to volume neurotransmission by means of extrasynaptic receptors.

**KEYWORDS**
amacrine cells, ankyrin-G, axon, axon initial segment, retina

## 1 | INTRODUCTION

In his early conceptualization of the "law of dynamic polarization" and what we now call the neuron theory, Cajal was troubled by the finding that amacrine cells ("spongioblasts") in the retina and granule cells in the olfactory bulb lacked an axon (Cajal, 1892, 1894; for review, see Shepherd, 1991). As Cajal did not believe that dendritic conduction differed from conduction in an axon, it was presumably the direction

of the nervous conduction of electrical impulses in relation to the cell body that posed a challenge for a general theory. The technique of intracellular recording later revealed that whereas neurons in the distal retina (photoreceptors, horizontal and bipolar cells) primarily signal with sustained, graded electrical potentials, neurons in the proximal retina (amacrine and ganglion cells) generate action potentials. The functional logic of these distinct properties is generally considered to be that signaling via graded potentials is sufficient for neurons in the distal retina because they do not transmit signals over longer distances where regenerative action potentials are needed for repeated amplification (reviewed by Dowling, 2012). Whereas this argument clearly applies to retinal ganglion cells, it is more difficult to see how it applies to amacrine cells, at least to narrow-field amacrine cells with relatively small dendritic trees. Early work with intracellular recording from amacrine cells in mudpuppy retina found evidence for TTX-sensitive action potentials (mediated by voltage-gated Na$^+$ [Na$_v$] channels), both in the cell body and in the dendrites (Miller & Dacheux, 1976). This raised the question whether the action potentials are actively propagated or only serve as a local amplification mechanism (reviewed by Dowling, 2012). On the basis of different experimental systems, there is evidence both for local (dendritic) action potentials with no active propagation, as well as soma-initiated action potentials with active propagation in a centrifugal direction (salamander retina: Cook & Werblin, 1994; macaque retina: Stafford & Dacey, 1997). Mammalian amacrine cells with actively propagated action potentials belong to the polyaxonal amacrine cells (Dacey, 1989; Famiglietti, 1992a, 1992b; Greschner et al., 2014; Kolb et al., 1981; Vaney et al., 1988; Völgyi et al., 2001), which, in contrast to the majority of amacrine cells, display two distinct types of processes identified as dendritic and axonal.

The AII amacrine cell is a narrow-field, bistratified cell found in the mammalian retina and transmits visual signals under both scotopic and photopic conditions (reviewed by Demb & Singer, 2012). It was explicitly identified with unique morphological and circuit properties by Kolb and Famiglietti (1974) and intracellular recording of AII amacrines in cat and rabbit retina indicated a transient-sustained visual response (Dacheux & Raviola, 1986; Nelson, 1982). The transient visual response component was interpreted as evidence for amplification by Na$_v$ channels or voltage-gated Ca$^{2+}$ channels and later whole-cell patch-clamp recordings of AII amacrines in slices of rat retina demonstrated TTX-sensitive, low-amplitude action potentials (Boos et al., 1993). Although the bistratified morphology corresponds to the presence of two types of dendrites, lobular and arboreal, there is no evidence for an axon in AII amacrine cells (e.g., Strettoi et al., 1992), raising the question of the localization of Na$_v$ channels. Recently, combined morphological and physiological investigations revealed the existence of an axon initial segment (AIS)-like process in mouse AII amacrines (Cembrowski et al., 2012; Wu et al., 2011), characterized by discrete clustering of Na$_v$ channels (Na$_v$1.1; Kaneko & Watanabe, 2007) colocalized with a series of proteins typically found at the AISs of axon-bearing neurons (for review, see Leterrier, 2018). One example is the cytoskeletal linker protein ankyrin that associates with Na$_v$ channels (Srinivasan et al., 1988) and is located at AISs and nodes of Ranvier in myelinated axons (Kordeli

et al., 1995). The discrete AIS-like process corresponds to the previously described "morphologically distinct process" (MDP; van Wart et al., 2005) and is responsible for the spiking observed in AII amacrines (Cembrowski et al., 2012; Wu et al., 2011).

The functional role of spiking mediated by Na$_v$ channels in AII amacrine cells is unclear. In the rd1 mouse retina, Na$_v$ channels are involved in mediating oscillatory activity via burst firing of AIIs that is propagated to retinal ganglion cells (Borowska et al., 2011; Trenholm et al., 2012), but similar burst firing can also be observed in normal retina by hyperpolarizing the membrane potential of the AIIs, suggesting that the bursting is intrinsic to the AIIs and generated by interactions between voltage-gated conductances within these cells (Choi et al., 2014). If the Na$_v$ channels serve as a mechanism of signal amplification (cf. Tian et al., 2010), the presence of the AIS-like process raises the question of its potential pre- and/or postsynaptic relationships with bipolar, amacrine, and ganglion cells. Because functional connectivity in the inner plexiform layer of the retina is strictly related to the level of stratification, for example, as observed for the stratification and connectivity of ON- versus OFF-center bipolar and ganglion cells (Famiglietti & Kolb, 1976; Famiglietti et al., 1977; Nelson et al., 1978; Peichl & Wässle, 1981; for review, see Masland, 2004, 2012), we undertook a systematic characterization of the morphology of the AII amacrine AIS-like process in rat retina, including laminar localization, spatial orientation, and distribution as a function of retinal eccentricity.

## 2 | MATERIALS AND METHODS

### 2.1 | Animals and general aspects

General aspects of the methods have previously been described in detail (Hartveit, 1996). The use of animals in this study was carried out under the approval of and in accordance with the regulations of the Animal Laboratory Facility at the Faculty of Medicine at the University of Bergen (accredited by AAALAC International). Male and female albino rats (Wistar HanTac, bred in-house or purchased from Taconic Bioscience, Denmark) had ad libitum access to food and water and were kept on a 12/12 light/dark cycle. Animals used for cell injections in retinal slices were between 4 and 7 weeks postnatal. Two animals were used for immunolabeling of retinal wholemounts. One wholemount (from a 7-week-old female rat) was analyzed quantitatively and the results are reported in this study. A second wholemount (from a 4-week-old male rat) yielded qualitatively similar results, but was not analyzed quantitatively. Animals were deeply anesthetized with isoflurane (IsoFlo vet 100%; Abbott Laboratories) in 100% O$_2$ and killed by cervical dislocation. After removing the eyes, the retinas were dissected out (in HEPES-buffered extracellular solution) and used for slices or as wholemounts.

### 2.2 | Retinal slice preparation and live cell injection

Retinal slices were cut by hand with a curved scalpel blade at a thickness of ~100 to ~150 μm. The slices were visualized with a

conventional, upright microscope (BX51WI; Olympus) with a ×60 (.9 NA) water immersion objective (Olympus) and Dodt gradient contrast (DGC) optics (Luigs & Neumann) for contrast enhancement. The extracellular perfusing solution was continuously bubbled with 95% $O_2$– 5% $CO_2$ and had the following composition (in mM): 125 NaCl, 25 $NaHCO_3$, 2.5 KCl, 2.5 $CaCl_2$, 1 $MgCl_2$, 10 glucose, pH 7.4 (osmolarity ~300 mOsm).

Using a combination of transmitted light and epifluorescence optics (filter set 49011 with excitation filter ET480/40X, beam splitter T510lpxrxt, and emission filter ET535/50m; Chroma), visually targeted AII amacrine cells were impaled with sharp microelectrodes with the tip filled with 5 mM Alexa Fluor 488 ("Alexa 488," Thermo Fisher Scientific) dissolved in 200 mM KCl and backfilled with 200 mM KCl without dye. Microelectrodes were pulled (P-87; Sutter Instrument) from thin-walled borosilicate glass (OD, 1.0 mm; ID, .78 mm; BF100-78-10; Sutter Instrument). When filled with dye solution, the resistance of the injection pipettes typically ranged between 80 and 150 MΩ. For injection, the microelectrode was connected to an intracellular amplifier (SEC-05LX; NPI Electronic) in bridge mode, controlled by Patchmaster software (HEKA Elektronik; RRID: SCR_000034). With the pipette resistances used, we typically did not find it necessary to apply a retaining current to prevent leakage of dye. After successful impalement, cells were injected with a current of −500 pA for 3 min (~1 Hz; 900 ms on per cycle).

## 2.3 | Immunocytochemical labeling of slices with injected cells

After injection, slices were fixed at room temperature for 10–15 min in 4% paraformaldehyde in .1 M phosphate buffer (PB; .081 M $Na_2HPO_4$/.019 M $NaH_2PO_4$, pH 7.4). Following fixation, slices were washed three times (5 min each) in .01 M phosphate-buffered saline (PBS; .01 M PB with 8.76 g NaCl and .2 g KCl per liter, pH 7.4). Next, slices were incubated for 1 h at room temperature in antibody incubation solution consisting of PBS with 5% normal goat serum (NGS; Sigma-Aldrich), .5% Triton X-100 (Sigma-Aldrich), and .05% $NaN_3$. Slices were then incubated for three nights (at 4°C) with primary antibody (mouse anti-ankyrin-G or guinea pig anti-ankyrin-G; Table 1) in antibody incubation solution. After incubation, slices were washed three times (10 min each) in PBS and incubated with secondary antibody in antibody incubation solution (with .2% Triton X-100), either for 2 h at room temperature or overnight at 4°C. Secondary antibodies were purchased from Thermo Fisher Scientific and included

goat anti-mouse coupled to Alexa Fluor 594 ("Alexa 594," #A11032) or Alexa Fluor 647 ("Alexa 647," #A21236), and goat anti-guinea pig coupled to Alexa 594 (#A11076) or Alexa 647 (#A21450), used at a dilution of 1:1000. Subsequently, the slices were washed three times (15 min each) in PBS and mounted in SlowFade Diamond Antifade mountant (refractive index 1.42; Thermo Fisher Scientific, cat. number S36967) between two precision coverslips (.17 mm thickness; Karl Hecht Assistent, cat. number 1014/5024) separated by a .12 mm thick imaging spacer disk ("SecureSeal," cat. number 70327-13S; Electron Microscopy Sciences).

## 2.4 | Immunocytochemical labeling of retinal wholemounts

For immunolabeling of retinal wholemounts, we used a marker (Penol) to place a spot of permanent ink (xylene free) on the dorsal part of the eye before removing it from the orbit. After enucleation, we made a small cut in the dorsal part of the retina and sclera before dissecting the retina from the eye cup. The retina was then flattened by making four radial incisions from the periphery almost to the center and transferred onto the non-gridded surface of a piece of nitrocellulose filter paper (Millipore, cat. number HABG01300). The filter paper with attached retina was then positioned on a piece of folded tissue paper (e.g., Kimwipe) and a few drops of HEPES-buffered extracellular solution was added on top and allowed to soak through. For fixation, a few drops of 4% paraformaldehyde (in .1 M PB) was added on top and allowed to soak through. After repeating this 2–3 times, the filter paper with retina was transferred to a larger volume of 4% paraformaldehyde in .1 M PB and fixed for 30 min at room temperature. After fixation, the retina was washed six times (10 min each) in .01 M PBS and incubated in antibody incubation solution (identical to that used for slices) overnight at 4°C. The retina was then incubated for four nights (at 4°C) with primary antibodies (mouse anti-ankyrin-G and guinea pig anti-parvalbumin; Table 1) in antibody incubation solution identical to that used for slices, but with .2% Triton X-100. Afterwards, the retina was washed six times (10 min each) in PBS and incubated overnight (at 4°C) with secondary antibodies (goat anti-guinea pig coupled to Alexa 488, #A11073 from Thermo Fisher Scientific, diluted 1:1000; goat anti-mouse coupled to Alexa 594, #A11032 from Thermo Fisher Scientific, diluted 1:1000) in antibody incubation solution (identical to that used for slices, i.e., with .2% Triton X-100). Finally, the retina was washed six times (10 min each) in PBS and mounted in Vectashield between a microscope slide and a precision

**TABLE 1** Primary antibodies

| Antibody name | Immunogen | Source, cat #, RRID | Antibody type | Dilution |
|---|---|---|---|---|
| Ankyrin-G | Ankyrin-G (463) | Santa Cruz, SC12719, AB_626674 | Mouse, monoclonal | 1:100 |
| Ankyrin-G | Ankyrin-G epitope: aa 1784-1961 rat, mouse | Synaptic Systems, 386004, AB_2725774 | Guinea pig, polyclonal | 1:1000 |
| Parvalbumin | Parvalbumin, aa 1-133 rat | Synaptic Systems, 195004, AB_2156476 | Guinea pig, polyclonal | 1:1000 |

Abbreviation: RRID, Research Resource Identifiers (for details see the Resource Identification Portal: https://scicrunch.org/resources).

coverslip separated by spacers made of small pieces of coverslip glass (∼.17 mm thickness) glued to strips of .12 mm thick imaging spacer disks.

## 2.5 | Antibody characterization

All primary antibodies used in this study have been validated by the commercial providers and, as indicated in their supplier's data sheet, showed a band of the respective molecular weight of the protein detected, as revealed by Western blot. Antibodies are identified by their Research Resources Identifiers (RRIDs) (Table 1).

## 2.6 | Confocal microscopy and image acquisition

Retinal tissue was imaged on a TCS SP8 confocal microscope (Leica) equipped with HyD detectors. All image stacks were acquired at 8-bit resolution and acquisition was controlled by LAS X software (Leica). For imaging of immunolabeled slices with injected cells, we used a ×93 glycerol immersion objective (HC PL APO CS2, 1.3 NA; Leica). We used the "white light" laser and acousto-optic filters to obtain the following excitation laser lines: 488 nm (for Alexa 488), 594 nm (for Alexa 594), and 647 nm (for Alexa 647). The emission bandwidths for the corresponding channels were set to 500–550, 600–630, and 660–750 nm, respectively. For both slices and wholemounts, the laser intensity for each of the two acquisition channels was adjusted to maximize the dynamic range, with minimal saturation at the highest intensities. For injected cells, each image stack was acquired as a series of optical slices (each slice with 1816 × 1816 pixels) by sequential scanning (between lines) of the different channels. For each of the two frames (corresponding to the two channels), each line was scanned two times and accumulated to increase the signal-to-noise ratio (SNR). The confocal pinhole was set to .5 Airy units (calculated for 580 nm light). To obtain well-sampled image stacks that could be processed with deconvolution (see "Image deconvolution" below), images were sampled at a rate slightly higher than the ideal Nyquist rate. The Nyquist sampling distance in the lateral direction was calculated as:

$$\Delta_x = \Delta_y = \frac{\lambda_{eff}}{4n \times \sin\alpha} \tag{1}$$

and for the axial direction, the Nyquist sampling distance was calculated as:

$$\Delta_z = \frac{\lambda_{eff}}{2n \times (1 - \cos\alpha)} \tag{2}$$

where $\lambda_{eff} = 1 / \left( \frac{1}{\lambda_{ex}} + \frac{1}{\lambda_{em}} \right)$, $\lambda_{ex}$ is the wavelength of the excitation light, $\lambda_{em}$ is the wavelength of the emission light, $n$ is the lens medium refractive index (1.45 for the glycerol used for immersion), and $\alpha$ is the half-aperture angle of the objective (reviewed by

Heintzmann, 2006; see also https://svi.nl/NyquistRate). For the digital zoom and the number of pixels in each image slice, the XY pixel size was ∼46 nm and the focal plane interval was ∼150 nm. All values were sufficient to satisfy Nyquist rate sampling according to the stated equations.

For imaging immunolabeled wholemount preparations, we used a ×63 glycerol immersion objective (HC PL APO Glyc corr CS2, 1.3 NA; Leica). Imaging was performed as described above for slices, except that we used the Navigator module of the Leica LAS X software to acquire a total of 16 image stacks arranged roughly along two orthogonally oriented lines across the retina (see Results). Each image stack was acquired as a series of optical slices (260–359 slices in each stack, each slice 5352 × 5352 pixels). The XY pixel size was ∼46 nm and the focal plane interval (Z) was ∼150 nm, sufficient to satisfy Nyquist sampling according to the stated equations. Excitation laser lines and emission bandwidths (for Alexa 488 and 594) were identical to those used for imaging slices.

## 2.7 | Image deconvolution

Huygens Essential (version 18 and 19, 64 bit, Scientific Volume Imaging; RRID:SCR_014237) was used to digitally deconvolve each channel of an image stack to remove noise (effectively increasing the SNR) and decrease axial and lateral blurring. The software reassigned out-of-focus light with a theoretically calculated point spread function, using the classic maximum likelihood estimation (CMLE) deconvolution algorithm. For each image stack, we estimated an optimal value for the user-selectable SNR parameter by repeating the deconvolution for several values of the SNR while keeping all other parameters and settings constant (see Zandt et al., 2017). The optimal SNR was determined separately for each channel and the deconvolved image stacks were recombined as a dual-channel stack for subsequent analysis. For image stacks of injected cells in immunolabeled slices, the SNR values for the two channels were between 5 and 7 for the injected AII and between 5 and 10 for the ankyrin-G-labeled processes. For image stacks acquired from wholemounts immunolabeled for parvalbumin and ankyrin-G, the SNR values were between 2 and 5, and between 1 and 7, respectively.

## 2.8 | Morphological reconstruction and analysis

Quantitative morphological reconstruction of fluorescently labeled cell bodies and processes in wholemounts was performed using computer-aided neuronal tracing software (Neurolucida 360, version 2018 and 2019, 64-bit, MBF Bioscience; RRID:SCR_016788), running on a PC equipped with a graphics tablet (Cintiq 22HD, Wacom). For cells injected with fluorescent dye and immunolabeled for ankyrin-G, the immunolabeled process was reconstructed in three dimensions (3D). As detailed below, we obtained three separate reconstructions (referred to as reconstructions A, B, and C), using two different reconstruction methods.

For reconstruction A, we used the manual tracing mode of Neurolucida 360 to obtain a reconstruction of the dye-filled process, starting from the first branch point proximal ("upstream") to the ankyrin-G-labeled segment and ending at the distal tip (terminal) of the process. We used the "marker" function in Neurolucida 360 to indicate the proximal and distal ends of the ankyrin-G-labeled segment and associated the two markers with the reconstructed process (A; "attach" function in Neurolucida 360). We used reconstruction A and the associated markers for morphometric analysis to provide information about the distance from the proximal branch point (node) to the beginning and end of the ankyrin-G-labeled segment. We next obtained a separate reconstruction (B) of the ankyrin-G-labeled segment in isolation by duplicating reconstruction A and removing the reconstruction points before (upstream) and after (downstream) the proximal and distal ends of the ankyrin-G-labeled segment, respectively. For each process, the origin (beginning) was defined as the part anatomically closest (i.e., along connected processes) to the apical dendrite (or soma) and the ending was defined as the distal terminal. To generate reconstruction C, we used the semi-automatic ("user-guided") tracing mode with 3D visualization in Neurolucida 360 (identical to the method used to reconstruct ankyrin-G-labeled processes in wholemount retina, see below). We used reconstructions B and C to provide information about properties inherent to the ankyrin-G-labeled process itself (e.g., length, surface area, volume, etc.) and for comparison with the morphological analysis of the immunolabeled wholemount retinas (where only the ankyrin-G-labeled processes could be reconstructed). The reconstructions were not corrected for shrinkage.

For morphological analysis of immunolabeled retinal wholemounts, we first segmented the cell bodies of AII amacrine cells labeled for parvalbumin (Wässle et al., 1993). This was done by manually tracing the contour of the cell body, with the focal plane adjusted according to the image slice with the largest cross-sectional area observed for each cell individually. Three morphological characteristics allowed us to distinguish between AII amacrines and the non-AII parvalbumin-positive cell population in this location of the rat retina (Wässle et al., 1993). First, the intensity of labeling is lower for AII amacrine cells than for the other cell population. Second, the cell bodies of the non-AII population are located slightly more distally in the retina (i.e., closer to the outer plexiform layer) than the AII cell bodies. Third, whereas AII amacrine cells typically have a thick apical dendrite (parvalbumin-positive) that extends vertically into the inner plexiform layer, the somata of the non-AII amacrine cells extend a number of (parvalbumin-positive) processes that run laterally for some distance before they descend towards stratum 5 (S5) of the inner plexiform layer.

After delineating all cell bodies corresponding to AII amacrine cells in an image stack, we used Neurolucida 360 to automatically position a marker within each cell body contour, located at the XYZ coordinate of the center-of-mass (centroid) of the contour. After processing the morphological reconstructions with analysis functions in Neurolucida Explorer (versions 2018 and 2019, 64-bit, MBF Bioscience; RRID: SCR_017348), the results were analyzed with IGOR Pro (version 7 and 8; WaveMetrics; RRID:SCR_000325). We computed the Dirichlet (Voronoi) domains (including their areas) and the nearest-neighbor distances for the population of XY coordinates corresponding to the centroids of the AII amacrine cell bodies. When computing the nearest-neighbor distances, we only took into account the XY coordinates and ignored differences between the Z coordinates. The regularity index for a given distribution of AII cell bodies was calculated as the ratio between the mean and SD of the nearest-neighbor distances for a given region (image stack; Wässle & Riemann, 1978). In addition, MATLAB (version 2019a; The Mathworks; RRID:SCR_001622) was used to calculate the number of nearest neighbors for each cell, corresponding to the number of edges in each Dirichlet domain. Nearest-neighbor distances and regularity indices for origins and endings of ankyrin-G-labeled processes (see below) were calculated in the same way.

For analysis of the ankyrin-G-labeled processes in the wholemount image stacks, we reconstructed all labeled processes that were identified as having the morphology typical of AIS-like processes belonging to AII amacrine cells (see Results), irrespective of whether a given process (in whole or partially) was located in the inner nuclear layer, inner plexiform layer or ganglion cell layer. For three stacks, we reconstructed all ankyrin-G-labeled processes, irrespective of the morphology. For these three stacks, each ankyrin-G-labeled process was "tagged" according to its identity as an AII-type or a non-AII-type process. To reconstruct a labeled process, we used the 3D visualization in Neurolucida 360 and the semi-automatic tracing mode (as for reconstruction C, see above). For processes that displayed visible asymmetry, that is, with a terminal swelling at one end, the origin (beginning) was set to the end with the smaller diameter and the ending was set to the end with the terminal swelling. In some cases, as judged by eye, the semi-automatic tracing did not generate an adequate result and it was necessary to manually trace the process, partly or in whole. Ankyrin-G labeling was membrane limited and with the high resolution used for imaging appeared as a hollow tube, particularly toward the terminal swelling. Because the semi-automatic tracing mode of Neurolucida 360 cannot properly reconstruct this as a single process, we used the "morphological closing tool" (corresponding to spatial low-pass filtering) in Neurolucida 360 to close any gaps between the membrane-delimited labeling before reconstruction. Neurolucida Explorer was used to analyze all reconstructed ankyrin-G-labeled processes with respect to length, surface area, volume, and length-weighted average diameter. The reconstructions were not corrected for shrinkage.

Tortuosity of a reconstructed process was calculated as the ratio between the distance along the process, that is, the anatomical distance of the path from the origin to the ending, divided by the straight-line (Euclidean) distance between the same points. Accordingly, the smallest possible tortuosity is 1, which is the tortuosity of a straight line (path). With increasing complexity of the path between origin and ending, the tortuosity increases.

## 2.9 | Density estimates

For morphological reconstructions of parvalbumin-labeled AII cell bodies and ankyrin-G-labeled cell processes in wholemount, we only

included elements that were fully included within the boundary (frame) of each acquired confocal stack. Unfortunately, this will under-estimate the corresponding spatial densities. To compensate for this, we also counted immunolabeled cell bodies intersected by the top or left edge of the image frame, as long as they were considered to unequivocally belong to AII amacrine cells. For cell bodies where we were uncertain if they belonged to AII amacrines or not, we included every other cell in the population of AIIs. For the ankyrin-G-labeled processes, no corresponding correction was performed.

## 2.10 | Tracing borders between retinal layers for stratification analysis

For stratification analysis of image stacks from wholemounts, the bor-ders between the inner nuclear layer and the inner plexiform layer and between the inner plexiform layer and the ganglion cell layer were traced at regular intervals through each stack using Neurolucida 360. IGOR Pro was then used to subdivide the inner plexiform layer into five equally thick strata (S1–S5) by calculating the vertical distance from each reconstruction point of the reconstructed border between the inner nuclear layer and the inner plexiform layer to the reconstructed border between the inner plexiform layer and the gan-glion cell layer, and generating additional contours located at 20%, 40%, 60%, and 80% of the distance between the borders (with 0% corresponding to the border between the inner nuclear and the inner plexiform layer). This was repeated for each vertical "slice" where the borders had been traced. For each image stack, the subvolume corresponding to each layer and stratum was demarcated by a "closed surface" as defined in Neurolucida 360. Unfortunately, the closed sur-face analysis available in Neurolucida Explorer does not by default report the location of the origins and endings of reconstructed processes. To circumvent this and obtain information about the loca-tion and stratification of origins and endings of reconstructed ankyrin-G-labeled processes, we used IGOR Pro to generate two separate "point" objects (0–.7 μm in length) for each reconstructed process, with each object located at the 3D position of the origin or ending. After importing these objects to the Neurolucida 360 environment, they were available for the "closed surface analysis" function in Neu-rolucida Explorer.

## 2.11 | Analysis of nearest-neighbor distance distributions

We generated histograms of nearest-neighbor distance distributions (bin width set to 1 μm) and fitted each histogram with a Gaussian function (IGOR Pro):

$$y = y_0 + A \times e^{-((x-x_0)/w)^2} \tag{3}$$

where $y_0$ is the baseline (fixed at 0), $A$ is the amplitude, and $w$ (width) is equal to $\sqrt{2} \times$ SD. For each population of XY coordinates used to calculate nearest-neighbor distances, we also calculated the expected probability density function for a randomly distributed population with the same spatial density (cf. Wässle & Riemann, 1978):

$$P(r) = 2\pi\lambda r \times e^{-\lambda\pi r^2} \tag{4}$$

that is, the probability of finding the nearest neighbor at a distance $r$ from an arbitrarily chosen point in a random point pattern with den-sity equal to $\lambda$. Because our data are represented in absolute, and not relative, frequency histograms where the integral is equal to the total number of points in a given region, we converted the probability den-sity distribution $P(r)$, where the integral is equal to 1, by multiplying with the total number of points ($n$) in a given region before the corresponding function was compared with a given observed distribution:

$$n \times P(r) = n \times 2\pi\lambda r \times e^{-\lambda\pi r^2} \tag{5}$$

where the density $\lambda$ is given by $n/A$ where $A$ is the area of each acquired region (246.03 × 246.03 μm²).

## 2.12 | General data analysis and presentation

For data analysis and visualization, we used Huygens Essential, Neu-rolucida Explorer, IGOR Pro, MATLAB, and Excel. Experimental data are presented as means ± SD ($n$ = number of cells, reconstructed processes or points). For correlation analysis, we calculated Pearson's correlation coefficient $R$ and report the coefficient of determination, that is, the squared value $R^2$.

## 3 | RESULTS

### 3.1 | Morphology of ankyrin-G-labeled process of injected AII amacrine cells

To characterize the morphological properties of the ankyrin-G-labeled process of AII amacrine cells, we first combined intracellular injection of visually targeted and identified AIIs with immunolabeling for ankyrin-G. Our goal was to establish a set of morphological criteria that could be used for identifying ankyrin-G-labeled processes belong-ing to AII amacrines in retinal tissue, independently of an AII-specific cellular marker.

Using sharp microelectrodes, we injected AII amacrine cells in live in vitro slices with the fluorescent dye Alexa 488. Cells were visually targeted for injection using the same criteria as described in detail in previous studies from our laboratory (e.g., Zandt et al., 2017). When a cell was adequately filled with Alexa 488 and the fluorescent mor-phology verified that it was an AII amacrine, the slice was fixed and immunolabeled for ankyrin-G. Immunolabeling identified a clear ankyrin-G-labeled process in 43 of 48 successfully injected and processed AII amacrine cells. During morphological reconstruction of

the process immunolabeled for ankyrin-G, one cell displayed an ankyrin-G-labeled process that seemed to have been truncated (at the surface of the slice). This cell was excluded from further analysis and the results are reported for 42 AII amacrine cells. Because we used sharp microelectrodes for the injection, we were not able to obtain adequate electrophysiological responses from the same cells. Therefore, we do not know if any of the injected cells expressed $Na_v$ channels, irrespective of whether an ankyrin-G-labeled process could be identified or not. In ordinary whole-cell recordings of AII amacrine cells, evidence for such channels can be readily observed as depolarization-evoked action currents (e.g., Mørkve et al., 2002).

The four representative injected cells illustrated in Figure 1(a)–(d) display the typical morphology of AII amacrine cells (cf. Zandt et al., 2017), with a soma located at the border between the inner nuclear and inner plexiform layer, a thick apical dendrite that descends into the inner plexiform layer, and arboreal and lobular dendrites in the inner (proximal) and outer (distal) regions of the inner plexiform layer, respectively. In addition, each cell displays a relatively short process that is immunolabeled for ankyrin-G and ends in a terminal swelling (Figure 1(a)–(h)). Despite some morphological variability between cells, there were several characteristic morphological features of this process and its ankyrin-G-positive segment. For the following morphological description and analysis, we will refer to the schematic of an ankyrin-G-labeled process illustrated in Figure 1(i). The transition from the unlabeled to the ankyrin-G-labeled segment was relatively abrupt at the origin (i.e., the proximal end closest to the cell body, corresponding to location 2 in Figure 1(i)). For 20 cells (randomly selected from cells without branching of the ankyrin-G-labeled process and where the ankyrin-G-labeled segment did not start directly at a branch point), we measured a spatial profile of labeling intensity along the ankyrin-G-labeled process. When we measured the 10%–90% rise distance, that is, the distance over which the labeling intensity changed from background to full intensity, it was .44 ± .27 μm (range .19–1.28 μm; $n = 20$ profiles). This end of the ankyrin-G-labeled segment was relatively thin. For all processes, we measured the thickness of the proximal part of the ankyrin-G-labeled process (corresponding to location 2 in Figure 1(i)) directly from the deconvolved confocal image stack, taken as the full width at half maximum (FWHM) of the cross-sectional intensity profile. The average FWHM was .35 ± .11 μm (range .25–.78 μm, $n = 42$ processes). From the origin, the process continued along a more or less tortuous path before the terminal swelling (Figure 1(e)–(h)). Particularly at the distal end, but also at some intermediate locations, the ankyrin-G labeling appeared distinctly membrane-delimited, with an unlabeled region in the center of the process (Figure 1(e)–(h)). This is illustrated in detail in Figure 1(j) that displays the distal part of the process in Figure 1(f) at higher magnification and in Figure 1(k) that displays spatial fluorescence intensity profiles (corresponding to the location of the arrow in Figure 1(j)) for Alexa 488 (used to fill the cell) and for the ankyrin-G labeling. For the majority of AIS-like processes, the ankyrin-G labeling extended almost to the very distal tip of the process (corresponding to locations 3 and 4 in Figure 1(i), respectively).

Whereas the ankyrin-G labeling typically extended into the terminal expansion (Figure 1(a)–(h)), we also observed a few cells where this was not the case. For the two examples illustrated in Figure 2, the fluorescence of Alexa 488 (intracellularly injected) visualized a process with a clear bulb-like ending (Figure 2(a), (d)). Both processes also displayed clear immunolabeling for ankyrin-G (Figure 2(b), (e)), with the corresponding fluorescence extending towards the distal end of the process, but essentially disappearing at the point where the process expanded into the bulb-like swelling (Figure 2(c), (f)).

For all 42 cells, we could trace the process with ankyrin-G labeling further upstream, either to a node (i.e., a branch point) or directly to the soma. In a few cases, the process with ankyrin-G labeling originated directly from the soma ($n = 3$ cells) or apical dendrite ($n = 3$ cells), but more typically it originated from a branch point (corresponding to location 1 in Figure 1(i)) along a lobular dendrite ($n = 29$ cells) or an arboreal dendrite ($n = 7$ cells). Branching of the ankyrin-G-labeled process was relatively rare. In our material, it was observed for only nine of 42 reconstructed processes, with a side branch typically appearing as a short, slender, spine-like process connected to the main process. In five of the nine cases, the small side branch was also labeled for ankyrin-G.

We generated morphological reconstructions of the complete process that contained the segment with ankyrin-G labeling (between locations 1 and 4 in Figure 1(i); reconstruction A) and of the ankyrin-G-labeled segment itself (between locations 2 and 3 in Figure 1(i); reconstruction B; $n = 42$ cells). The reconstructions were then used to obtain quantitative data for a series of morphological properties: anatomical length (the distance between locations 2 and 3 in Figure 1(i)), surface area, volume, diameter, tortuosity, distance from proximal border of ankyrin-G labeling (location 2 in Figure 1(i)) to the nearest upstream node (location 1 in Figure 1(i)), and distance from distal border of ankyrin-G labeling (location 3 in Figure 1(i)) to the distal tip of the process (location 4 in Figure 1(i)). The results are illustrated in Figure 3(a)-(g). When the processes were sorted based on length, the distribution varied smoothly between the minimum and maximum (Figure 3(a)). With the same sorting order, the distribution of surface area and volume was less smooth (Figure 3(b), (c)), but both parameters were positively correlated with length, with stronger correlation for surface area ($R^2 = .633$) than for volume ($R^2 = .198$). For almost every process, the average (length-weighted) diameter (.44 ± .10 μm, range .26–.82 μm) was closer to the minimum than to the maximum diameter (1.16 ± .35 μm, range .55–2.03 μm), reflecting the relatively constant thickness of the process from its origin until the expansion at the distal end (Figure 3(d)). For the diameter measurements in Figure 3(d), we constrained the minimum diameter to .2 μm because of the limited resolution of confocal light microscopy.

The majority of ankyrin-G-labeled processes appeared relatively straight, but some displayed a more complex and convoluted path, even to the extent of curving around the soma or apical dendrite (Figure 1(d)). We quantified this property by calculating the tortuosity (for definition, see Materials and Methods). The majority of processes had a tortuosity between 1 and 1.5 ($n = 32$ processes; Figure 3(e)),

corresponding to a relatively straight path, but a few processes displayed a tortuosity between 2 and 3 (n = 4 processes; Figure 3(e)). For the population as a whole, the average tortuosity was 1.43 ± .42 (range 1.10–2.82; n = 42).

For the large majority of cells, the start of the ankyrin-G labeling occurred at some distance from the nearest upstream node (i.e., branch point from a dendrite or the soma). In only two cases did the ankyrin-G labeling start directly at the node (corresponding to no
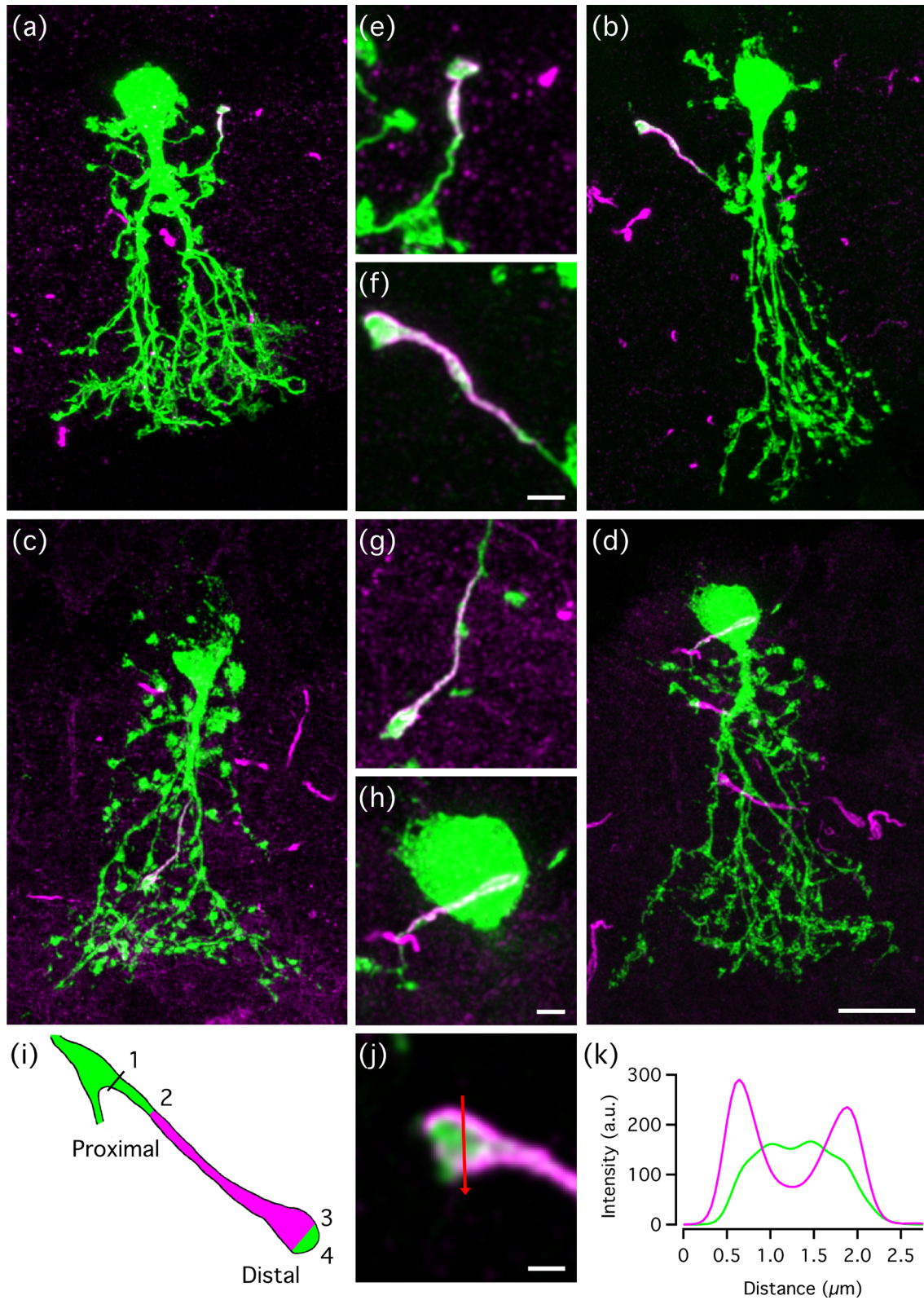


**FIGURE 1**    Legend on next page.

separation between locations 1 and 2 in Figure 1(i)). The distance from the start of ankyrin-G labeling to the upstream node typically was just 2–6 μm, but could range up to 12 μm (Figure 3(f)), with a mean value of 3.3 ± 3.2 μm (range 0–12.3 μm; $n = 42$ cells). For 41 of 42 cells, the length of the unlabeled distal segment (corresponding to the distance between locations 3 and 4 in Figure 1(i)) was less than 1.3 μm, but for one outlier, the corresponding length was 5.6 μm (Figure 3(g)). The average length of this unlabeled segment was .33 ± .89 μm ($n = 42$ cells).

In addition to the ankyrin-G-labeled process that could be identified as belonging to the injected AII amacrine cell, we could identify a large number of other ankyrin-G-labeled processes in each slice. Some of these had morphological characteristics very similar to those of the process belonging to the injected AII amacrine, including the presence of a clear bulb-like expansion at one end (e.g., Figure 2(c), (f)). These processes could belong to other AII amacrine cells. However, in addition to ankyrin-G-labeled processes with these characteristics, we also observed a number of labeled processes without a bulb-like ending.

From our analysis, it could seem that the presence of a terminal, bulb-like expansion is close to a necessary condition for classifying an ankyrin-G-labeled process as belonging to an AII amacrine cell. To analyze this quantitatively, we plotted the maximum diameter within the distalmost part (≤5 μm; corresponding to the bulb) versus the average diameter of the proximal 50% of the total length. From the scatter plot displayed in Figure 3(h), it can be seen that the large majority of AII-type ankyrin-G-labeled processes conformed to the typical "club shape," with only 2–3 processes found close to the identity line. This raises the question whether the presence of a terminal swelling is a sufficient condition for classifying an ankyrin-G-labeled process as belonging to an AII amacrine cell. Although the analysis presented so far cannot justify this conclusion, we did notice that all other ankyrin-G-labeled processes with the characteristic terminal expansion displayed a morphology that appeared qualitatively similar to the corresponding processes belonging to the injected AII amacrine cells (Figure 1). Accordingly, for the subsequent, more extensive morphological analysis of ankyrin-G-labeled processes in wholemount tissue without injected AII amacrine cells, we hypothesized that all ankyrin-G-labeled processes with a terminal expansion belonged to AII amacrine cells. If the presence of a terminal swelling is both (close to) necessary and sufficient for an ankyrin-G-labeled process to belong to an AII amacrine cell, the numerical densities should match across the retina.

## 3.2 | Density and distribution of AII amacrine cells

For our analysis of putative AII-type ankyrin-G-labeled processes across the retina, an important goal was to relate their distribution to that of the cell bodies of AII amacrine cells, with the expectation of matching densities. Therefore, we combined immunolabeling of ankyrin-G with that of parvalbumin, a marker for AII amacrine cells in rat retina (Wässle et al., 1993). Immunolabeling for parvalbumin also labels a population of widefield amacrine cells with cell bodies in the inner nuclear layer, but these can be (relatively) easily distinguished from AII amacrine cells based on the intensity of labeling, the relative position of the cell bodies, and the morphology of the proximal dendritic processes (see Materials and Methods). For any given region of the retina, AII cells are more weakly labeled than the parvalbumin-positive widefield amacrine cells (Wässle et al., 1993). Figure 4(a) shows a composite low-resolution overview of a wholemount retina immunolabeled for parvalbumin. From this preparation, we acquired a series of image stacks at higher resolution. An example of a high-resolution image with parvalbumin-positive cell bodies is illustrated in Figure 4(b), taken from the area marked by a square in Figure 4(a). This image corresponds to the maximum intensity projection of a horizontal "slab" located close to the border between the inner nuclear and inner plexiform layers (with the red lines in Figure 4(c) indicating the top and bottom borders of the slab). The image shows a large number of relatively weakly labeled cell bodies of AII amacrine cells and a smaller number of more intensely labeled cell bodies of widefield amacrine cells (Figure 4(b)). Whereas multiple processes emanate laterally from the cell body of the parvalbumin-positive widefield amacrine cells, there is generally one process that is considerably thicker than the others and extends horizontally before descending into the inner plexiform layer. In contrast, the thick apical dendrite of AII amacrine cells almost always originates as a single process and descends vertically into the inner plexiform layer. This difference can be seen clearly in projections orthogonal to the one illustrated in Figure 4(b), corresponding to images and maximum intensity projections in the XZ plane (Figure 4(c), (d)).

To analyze the distribution of AII amacrine cells in the retina, we segmented their immunolabeled cell bodies contained within a total of 16 image stacks distributed across the retina as illustrated in Figure 5(a) (see Materials and Methods). From the segmented cell bodies, we calculated a series of morphological properties, including density, Feret maximum and minimum, cross-sectional area, Dirichlet

**FIGURE 1** Colocalization between AII amacrine cells and immunolabeling for ankyrin-G. (a-d) Maximum intensity projections of confocal image stacks of retinal slices with AII amacrine cells injected with Alexa 488 (green) and immunolabeled for ankyrin-G (magenta). Scale bar, 10 μm (a-d). Here and later, all confocal images were generated after deconvolution of digital data (for details, see Materials and Methods). Notice colocalization between AII amacrine cell and ankyrin-G labeling at a single process, the axon initial segment (AIS)-like process. (e-h) Enlarged images of AIS-like processes of AII amacrine cells in (a-d), respectively. Scale bars, 2 μm (e, f); 2 μm (g, h). (i) Schematic figure of AIS-like process of AII amacrine cell (green) with ankyrin-G-labeled segment (magenta). Attachment of process to parent dendrite (origin) at location 1. Locations 2 and 3 correspond to proximal and distal borders of ankyrin-G-labeled segment, respectively. Location 4 marks ending of process (distal tip). (j) Enlarged image with details of distal tip of AIS-like process of AII amacrine in (b) and (f). Red arrow (length 2.75 μm) across terminal swelling used to create intensity profiles displayed in (k). Scale bar, 1 μm. (k) Spatial fluorescence intensity profiles (measured in arbitrary units, a.u.) across image in (j) for intracellular Alexa 488 (green) and immunolabeled ankyrin-G (magenta) [Color figure can be viewed at wileyonlinelibrary.com]
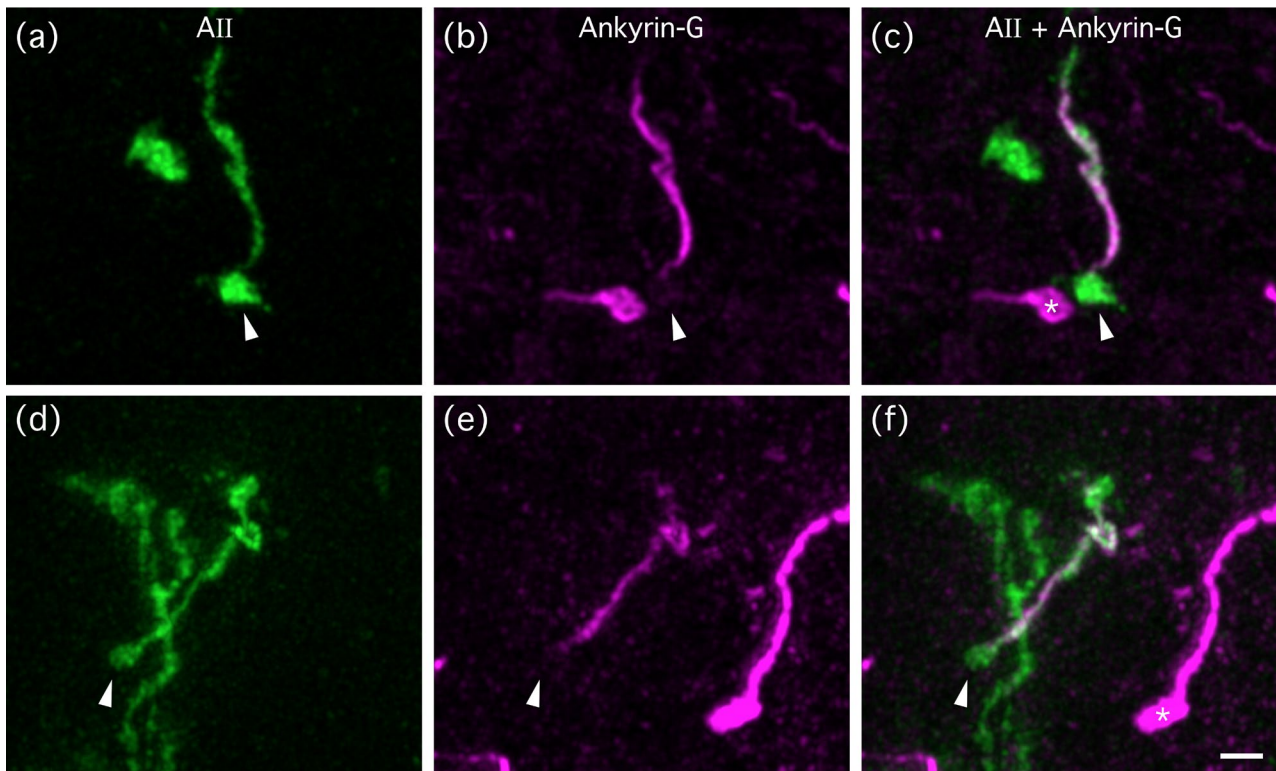
**FIGURE 2** For some AII amacrine cells, the ankyrin-G-labeled segment does not extend into the terminal swelling of the AIS-like process. (a-c) Colocalization between dye-injected AII amacrine cell and immunolabeling for ankyrin-G. Each image displays a maximum intensity projection of a confocal image stack with the AII amacrine cell injected with Alexa 488 (green, displayed separately in (a)) and immunolabeling for ankyrin-G (magenta, displayed separately in (b)), with overlay between AII and ankyrin-G signals in (c). Notice that the terminal swelling (arrow heads) of the AIS-like process in the injected AII is not labeled for ankyrin-G. The terminal swelling of a presumed AIS-like process (labeled for ankyrin-G) of another (non-injected) AII amacrine is marked by an asterisk in (c). (d-f) As in (a-c), but for a different AII amacrine cell. Scale bar, 2 μm (a-f) [Color figure can be viewed at wileyonlinelibrary.com]

domain area, nearest-neighbor distance, number of nearest neighbors, and regularity index (Figure 5(b)-(h)). Consistent with previous results reported by Wässle et al. (1993) for rat retina, we found that the density of AII amacrine cells was highest in the central and dorsal retina and decreased toward the periphery, with the most pronounced gradient found in the dorsal retina (Figure 5(b)). The highest density found was 5187 cells/mm$^2$, corresponding to the stack located most centrally in the dorsotemporal retina (Figure 5(b)).

The cell body size, measured by Feret maximum / minimum and cross-sectional area, displayed a center-periphery gradient with larger cell bodies toward the periphery, as well as a tendency toward slightly larger cell bodies in the dorsal than the ventral retina (Figure 5(c), (d)). The eccentricity-dependence of cell density was reflected in similar (but opposite) relationships for Dirichlet domain area and nearest-neighbor distance, such that the Dirichlet domain area and the nearest-neighbor distance increased toward the periphery, concomitant with the corresponding decrease in density (Figure 5(e), (f)). As for density, the larger gradients were found in the dorsal compared to the ventral retina. The number of nearest neighbors (estimated as the number of edges in the Dirichlet domains) was remarkably constant (at 5.9 or 6) across the retina (Figure 5(g)). The average nearest-neighbor distance regularity index for AII somata was 4.05 ± .33 (range 3.60–4.63; n = 16 image stacks), which is almost identical to the value reported by

Wässle et al. (1993). Despite the variability between different image stacks, there was no clear systematic difference between central and peripheral regions of the retina (Figure 5(h)).

In addition to calculating the regularity index from the mean and SD of the nearest-neighbor distances, we analyzed the corresponding distributions in more detail. For the four most central (#4) and four most peripheral regions (#1, Figure 6(a); locations illustrated in Figure 5(a)), the histograms that displayed the corresponding frequency distributions were well fitted by Gaussian functions (Figure 6(b), (c)). In contrast, the theoretical functions that displayed the expected random distributions for the identical spatial densities (cf. Wässle & Riemann, 1978) did not provide adequate fits to the observed distributions (Figure 6(b), (c)). However, as pointed out by Reese and coworkers, these results cannot be taken as evidence for a non-random distribution, as they do not take into account that the soma size will constrain the possible location of cell bodies when the density is relatively high (e.g., Keeley et al., 2020; Keeley & Reese, 2018).

## 3.3 | Morphology and distribution of ankyrin-G-labeled processes of AII amacrine cells

The same wholemount preparation that was immunolabeled for parvalbumin to detect AII amacrine cell bodies was also
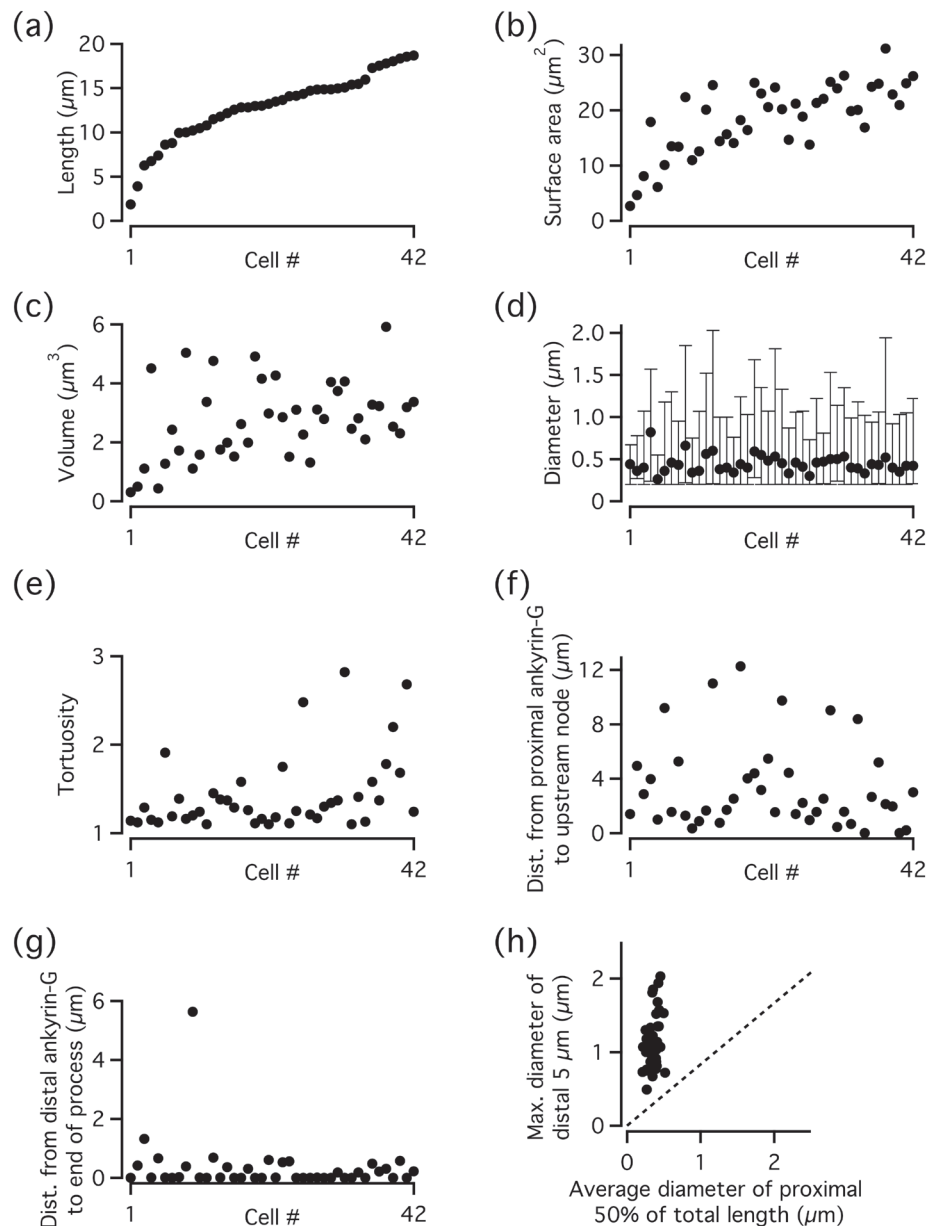
**FIGURE 3** Morphological properties of the AIS-like process of AII amacrine cells. For each dye-injected AII amacrine, the AIS-like process (immunolabeled for ankyrin-G) was morphologically reconstructed and analyzed according to the landmarks illustrated by the schematic in Figure 1(i). The parameters reported in (a-e) refer to the ankyrin-G-labeled segment between locations 2 and 3 in Figure 1(i). (a) Anatomical (non-Euclidean) length of ankyrin-G-labeled segment ($n = 42$), ordered from shortest to longest. (b) Surface area of ankyrin-G-labeled segment. Here and later, the processes are the same as in (a), and arranged according to the ordering in (a). (c) Volume of ankyrin-G-labeled segment. (d) Diameter of ankyrin-G-labeled segment, including average diameter (length-weighted; filled circles) and maximum and minimum diameter. Because of the limited resolution of light microscopy, the smallest possible diameter was set to .2 μm. (e) Tortuosity of ankyrin-G-labeled segment, calculated as the ratio between the anatomical distance along the process (the path from the origin to the ending), divided by the straight-line (Euclidean) distance between the same points. (f) Distance from proximal border of ankyrin-G-labeled segment (location 2 in Figure 1 (i)) to nearest upstream node (branch point; location 1 in Figure 1(i)). (g) Distance from distal border of ankyrin-G-labeled segment (location 3 in Figure 1(i)) to distal tip (location 4 in Figure 1(i)). (h) Scatter plot of relationship between maximum diameter of the distal 5 μm of ankyrin-G-labeled segment and average (length-weighted) diameter of the proximal 50% of the total length of the same process. The identity line (broken line) corresponds to equal values of the two diameters

immunolabeled for ankyrin-G to detect the AIS-like processes. Slender, ankyrin-G-labeled processes with varying length, but with no asymmetry between the two distal diameters, were found in both the nerve fiber layer and the ganglion cell layer, as well as at different heights (strata) across the inner plexiform layer (Figure 7(a)-(c)). The former are likely to be AISs of ganglion cells, whereas the latter could belong to bipolar and/or amacrine cells. Irrespective of the location, these processes could be clearly differentiated from ankyrin-G-labeled

processes with morphological properties that matched those described above for injected AII amacrine cells, most notably the presence of a terminal, bulb-like expansion (Figure 7(a)-(c)). These latter



(a)

(b)

(c)

(d)

INL

IPL

GCL

processes will be referred to as "AII-type" ankyrin-G-labeled processes. After manual identification, they were segmented by semi-automatic morphological reconstruction in Neurolucida 360 (Figure 7 (d)-(f)).

In several cases, we observed that AII-type ankyrin-G-labeled processes were labeled for parvalbumin as well, albeit weakly. Some representative examples are displayed in Figure 7(g)-(i). Typically, the strongest labeling for parvalbumin was observed in the terminal, bulb-like expansion. Although we were not able to use the labeling for parvalbumin to confidently trace a double-labeled process back to the labeled cell body of an AII amacrine cell, these observations support the hypothesis that ankyrin-G-labeled processes with AII-type morphology did indeed belong to AII amacrine cells.

Upon detailed examination, we also found several examples of processes belonging to the parvalbumin-positive, widefield (non-AII) amacrine cells that were immunolabeled for ankyrin-G in addition to parvalbumin. This analysis was easier to perform on image stacks sampled from the peripheral retina, where the overall density of labeled cells and processes was lower and where the labeling intensity tended to be higher. When the morphology of the parvalbumin-positive widefield cells was inspected in the horizontal (XY) plane, we often observed a particularly thick dendrite that could be followed for a considerable distance in the horizontal plane after it emanated from the cell body (Figure 8(a)). In addition, we could identify a number of much thinner processes that branched both from this process and
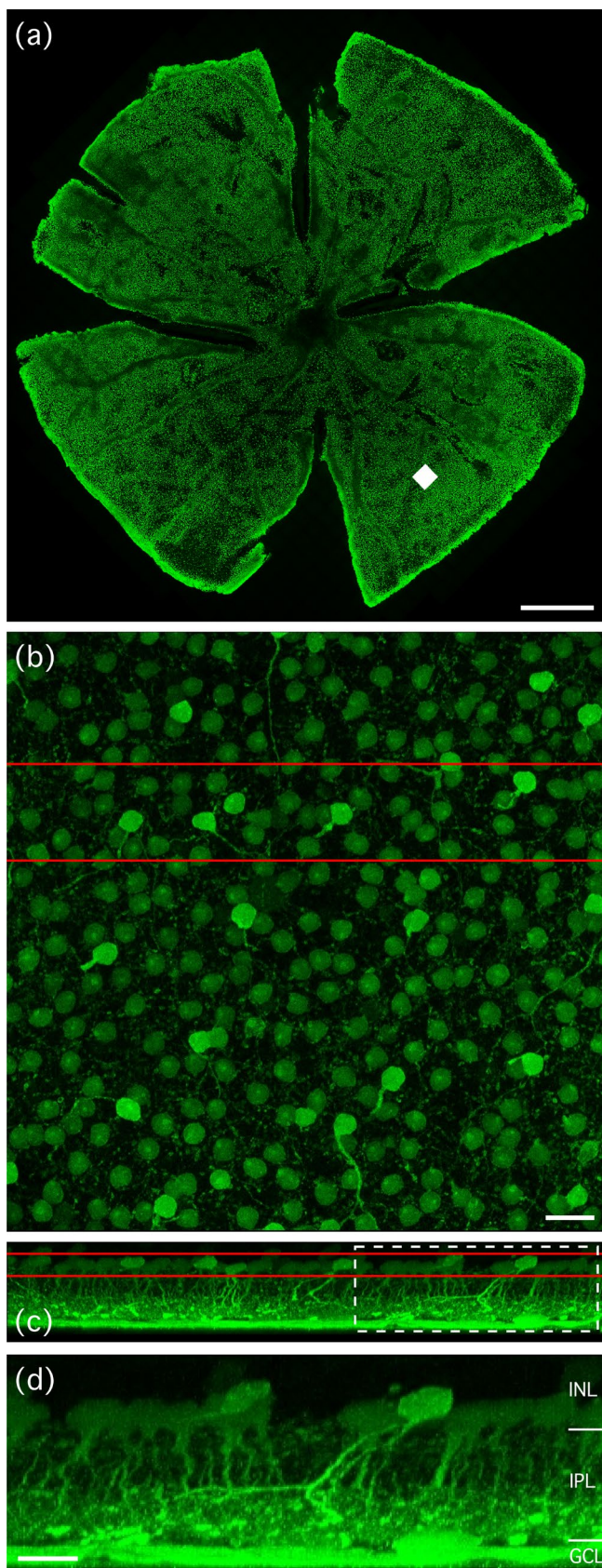
**FIGURE 4** Immunolabeling of parvalbumin-containing neurons in the retina. (a) Composite of low-resolution tiles (each 512 × 512 pixels) from confocal imaging (×63 objective, single focal plane, 944 images) of a wholemount retina immunolabeled for parvalbumin (and ankyrin-G). The white square corresponds to the size, location and orientation (in the XY plane) of the high-resolution confocal image stack illustrated in (b-d). Wholemount retina flattened by four radial incisions that divided the retina into quadrants. Scale bar, 1 mm. (b) Maximum intensity projection of horizontal (XY) slab of high-resolution confocal image stack. For all such stacks, the X × Y dimensions correspond to 246.03 × 246. 03 µm². The borders of the slab along the Z (depth) axis correspond to the distance between the red lines (8.25 µm) in the vertical (XZ) projection in (c). Notice the more frequent, relatively weakly labeled cell bodies, corresponding to AII amacrine cells, and the less frequent, relatively strongly labeled cell bodies, corresponding to a type of widefield amacrine cell. Also notice that a relatively thick process emanates in a lateral direction from many of the labeled widefield cell bodies. Scale bar, 20 µm (b, c). (c) Maximum intensity projection of vertical (XZ) slab of high-resolution confocal image stack (same as in (b)). The borders of the slab along the Y axis correspond to the distance between the red lines (39.17 µm) in the horizontal (XY) projection in (b). Rectangle marked by broken lines enlarged in (d). (d) Enlarged view with weakly labeled AII amacrine cells displaying vertically oriented apical dendrites and a strongly labeled widefield amacrine cell with a more obliquely oriented thick process running through the inner plexiform layer. Here and later, retinal layers and the borders between them are indicated by abbreviations and horizontal lines: INL, inner nuclear layer; IPL, inner plexiform layer; GCL, ganglion cell layer. Scale bar, 10 µm [Color figure can be viewed at wileyonlinelibrary.com]

directly from the cell body. In the cases where we observed processes double-labeled for parvalbumin and ankyrin-G that could be traced back to a parvalbumin-labeled widefield amacrine cell, they branched directly from the cell body and not from the thick dendrite. An example of such a process is illustrated in Figure 8(a)-(d). In no case did the ankyrin-G-labeled segment display a bulb-like expansion and it was never located close to the end of the process. We observed additional similar processes that were double-labeled for ankyrin-G and parvalbumin, but typically the labeling for parvalbumin was too weak to reliably trace them back to a labeled cell body. We did not observe any parvalbumin-labeled widefield amacrine cell with more than one ankyrin-G-labeled process.
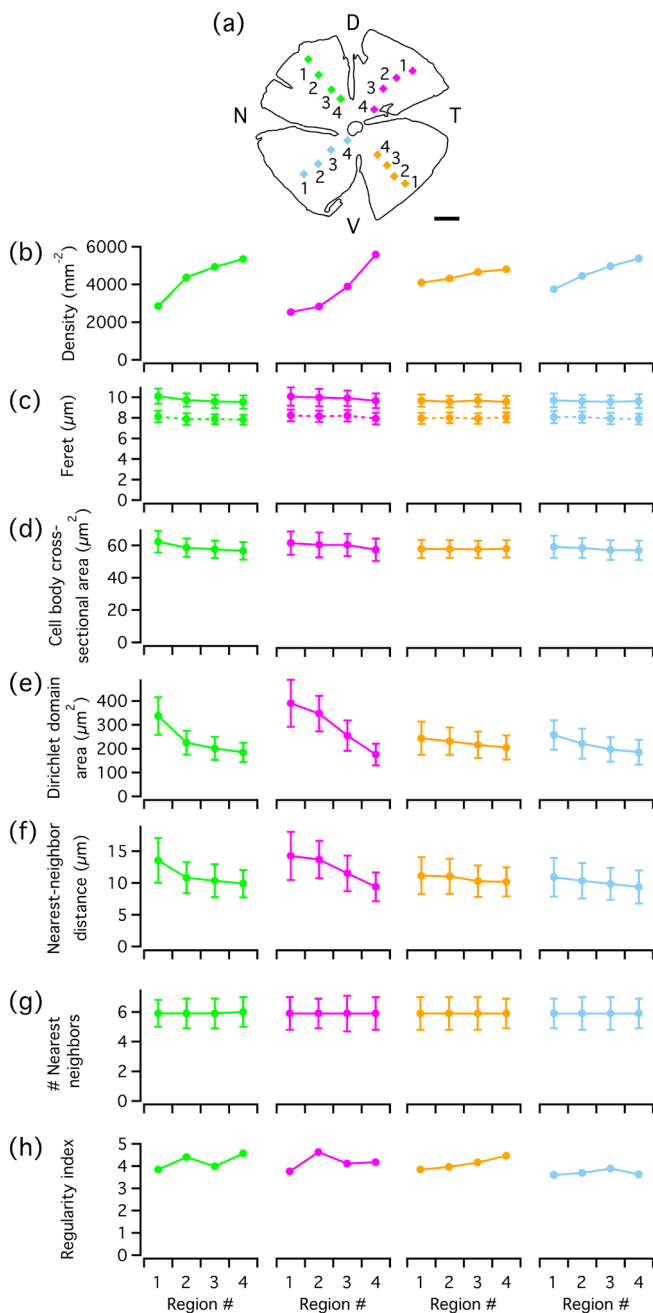
For three of the image stacks (as indicated in Figure 9(a)), we reconstructed all the ankyrin-G-labeled processes (both the AII-type and the non-AII-type) located in the inner nuclear, inner plexiform and ganglion cell layers. This made it possible to use the same analysis as in Figure 3(h) to examine if the manual separation of ankyrin-G-labeled processes into AII-type and non-AII-type resulted in non-overlapping populations. For the processes reconstructed in each of the three image stacks, we plotted the maximum diameter within the distal part (≤5 μm) versus the average diameter of the proximal 50% of the total length. Because the processes classified as non-AII-type during reconstruction did not display a strong asymmetry of the opposite end diameters, we defined proximal and distal for these processes as the ends with the smaller and larger average diameters, respectively. From the scatter plots for the individual image stacks (Figure 9(b)), it can be seen that there was relatively low overlap between processes classified as AII-type or non-AII-type. Whereas the diameter distribution for AII-type processes varied with retinal eccentricity, the distribution for non-AII-type processes appeared invariant with respect to eccentricity (Figure 9(b)). We also compared these scatter plots with the corresponding data for the ankyrin-G-labeled processes of the injected AII amacrine cells (from Figure 3(h)). Because we did not know the eccentricity of the dye-injected cells, we combined the data points for the three image stacks (Figure 9(c)). Although the large majority of data points for AII-type processes identified from dye-injected cells overlapped with the data points generated from processes identified as AII-type in the wholemount retina, a few (∼5) were located within the main region of non-AII-type processes (Figure 9(c)). For the three data points clearly located within the main



**FIGURE 5** Quantitative analysis of distribution and morphological properties of AII amacrine cells in wholemount retina immunolabeled for parvalbumin. (a) Schematic figure of wholemount retina (same as in Figure 4) and the location of the 16 high-resolution confocal image stacks used for counting and morphological analysis. Here and later, the size of each colored square corresponds to the relative size of the image stack (drawn to scale, X × Y dimensions correspond to $246.03 \times 246.03 \ \mu m^2$), each region (image stack) is numbered from 1 (most peripheral) to 4 (most central), and the orientation of the retina is indicated by capital letters denoting **D**orsal, **V**entral, **N**asal, and **T**emporal. Scale bar, 1 mm. (b) Spatial density of cell bodies as a function of retinal quadrant and eccentricity. Here and later, retinal quadrant and eccentricity are indicated by color and region number, respectively (as in (a)). (c) Feret maximum (continuous lines) and Feret minimum (broken lines) of the maximum cross-sectional area of the cell bodies (in the XY plane). Here and later, values are plotted as mean ± SD. (d) Cross-sectional area of the maximum circumference of the cell bodies (in the XY plane). (e) Dirichlet domain area for the population of XY coordinates (center-of-mass locations of cell bodies) within each region. (f) Nearest-neighbor distance for the population of XY coordinates (center-of-mass locations of cell bodies) within each region. (g) Number of nearest neighbors for the cells within each region (estimated from the Dirichlet domains). (h) Regularity index, calculated as the ratio between the mean and SD of the nearest-neighbor distances for each image stack [Color figure can be viewed at wileyonlinelibrary.com]
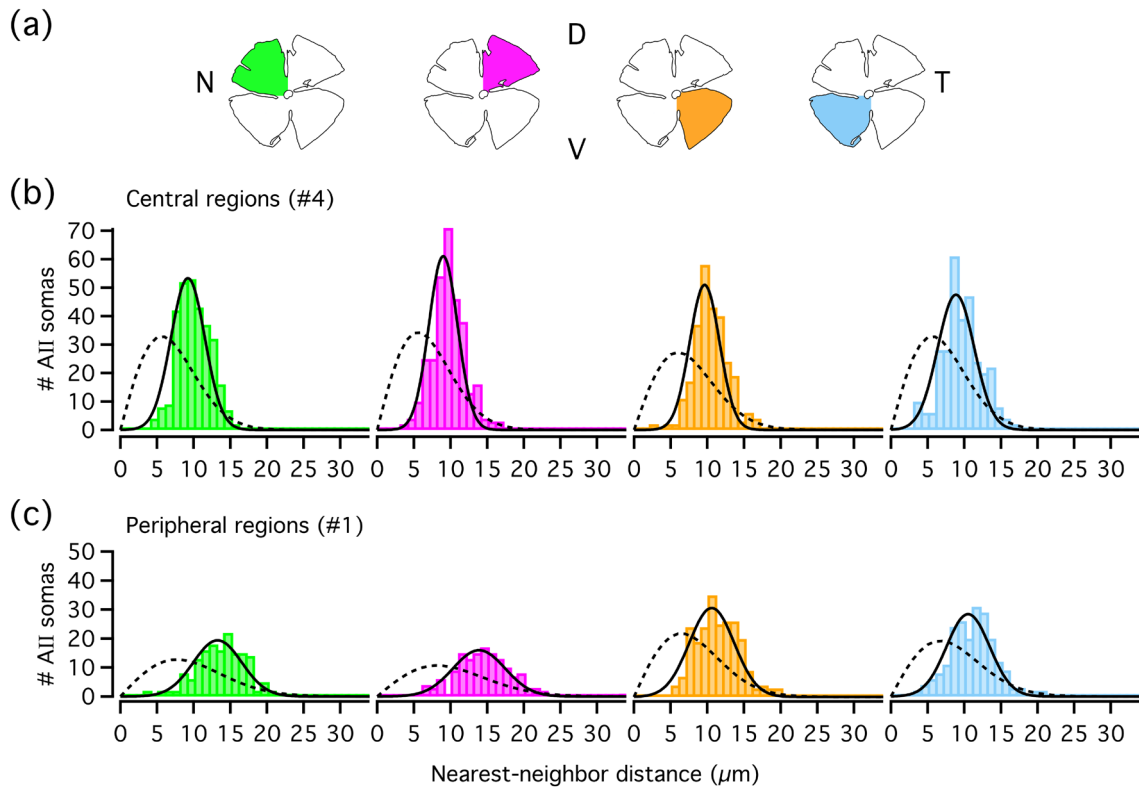
**FIGURE 6** Distribution of nearest-neighbor distances for AII cell bodies. (a) Schematic figures of wholemount retina. In all graphs (b, c), colors correspond to quadrant colors in (a) and region numbers correspond to those in Figure 5(a). (b) Frequency histograms displaying the distribution of nearest-neighbor distances for cell bodies within the most central region (#4) in each retinal quadrant. Each histogram has been fitted with a Gaussian function (equation 3; continuous black line). The broken black line in each panel shows the expected probability density function (multiplied by the total number of cells for a given region; equation 5) for a randomly distributed population of points (XY coordinates) with the same spatial density, but where the exclusion zones imposed by cell body size are ignored (for details, see Materials and Methods). (c) As in (b), but for the most peripheral region (#1) in each retinal quadrant [Color figure can be viewed at wileyonlinelibrary.com]

region of non-AII-type processes, the ankyrin-G labeling did not extend fully into the bulb-like terminal expansion (cf. Figure 3(h)). Two data points located at the border between the two populations of data points from wholemount labeling (AII- versus non-AII-type) displayed a typical bulb-like expansion. This suggests that when classification as AII-type versus non-AII-type is based on identifying a bulb-like terminal expansion, a small fraction of AII-type processes will be falsely classified as non-AII-type. From the material of dye-injected AII amacrine cells, the fraction of such processes might be ∼10% (4–5 out of 42 cells).

To further compare processes classified as AII-type and non-AII-type in the three image stacks (Figure 10(a)), we analyzed length, surface area, volume, and maximum diameter. As can be seen from Figure 10(b)-(e), there was considerable overlap between all properties except maximum diameter (Figure 10(e)). For surface area and volume, both influenced by maximum diameter, there was a larger difference between the averages of AII-type and non-AII-type processes in the most peripheral region (#1) compared to the more central regions (#2 and #4), but the degree of overlap was too large to use these properties to distinguish between the different type of processes.

We next analyzed a series of morphological properties for the AII-type ankyrin-G-labeled processes in all 16 image stacks across the retina (Figure 11(a)). For the retina as a whole, the density varied as a function of retinal eccentricity, with the largest gradient observed for the dorsal retina (Figure 11(b)). The density followed, but was consistently lower than, the density distribution for AII amacrine cell bodies, with the absolute magnitude of the difference larger towards the center of the retina (Figure 11(b)). Both length, surface area, volume, and maximum diameter decreased from the periphery towards the center, but there was considerable overlap between stacks from different retinal eccentricities (Figure 11(c)-(f)). The tortuosity was very similar across the retina (Figure 11(g)).

Our result of a regularity index of ∼4 for AII cell bodies (Figure 5(h), Figure 6) was very similar to that of Wässle et al. (1993). Although the distribution cannot be distinguished from a random distribution that takes into account the size of the cell bodies, we wanted to compare the results for AII cell bodies with the corresponding distributions (in the XY/horizontal plane) of the ankyrin-G-labeled AII-type processes. For this, we calculated the nearest-neighbor distances and the corresponding regularity indices for the origins and for the endings. The results for the endings are shown in Figure 11(h)

**FIGURE 7** Morphology of ankyrin-G-labeled processes in the inner plexiform layer. (a) Wholemount immunolabeled for ankyrin-G and parvalbumin. Maximum intensity projection of slab (thickness 31.2 μm, containing the entire inner plexiform layer and the proximal inner nuclear layer) of confocal image stack displaying immunolabeling for ankyrin-G (magenta). The square regions demarcated by white borders are displayed at higher resolution in (b) and (c). (b, c) Detailed view of ankyrin-G-labeled processes. Notice the terminal swellings displayed by a number of processes with morphology similar to those identified for dye-injected AII amacrine cells (Figure 1). (d) Same image as (a), after morphological reconstruction of all ankyrin-G-labeled processes displaying a terminal swelling. The square regions demarcated by white borders are displayed at higher resolution in (e) and (f). Scale bar, 20 μm (a, d). (e, f) Detailed view of ankyrin-G-labeled processes and reconstructions. Scale bar, 5 μm (b, c, e, f). (g-i) Examples of colocalization between parvalbumin-labeled processes belonging to AII amacrine cells and immunolabeling for ankyrin-G. Each image displays a single slice of a confocal image stack with immunolabeling for parvalbumin (green, displayed separately in (g)) and ankyrin-G (magenta, displayed separately in (h)), with overlay between AII and ankyrin-G signals in (i). Notice that for four processes, there is colocalization between parvalbumin and ankyrin-G (arrow heads). Scale bar, 5 μm (g-i) [Color figure can be viewed at wileyonlinelibrary.com]
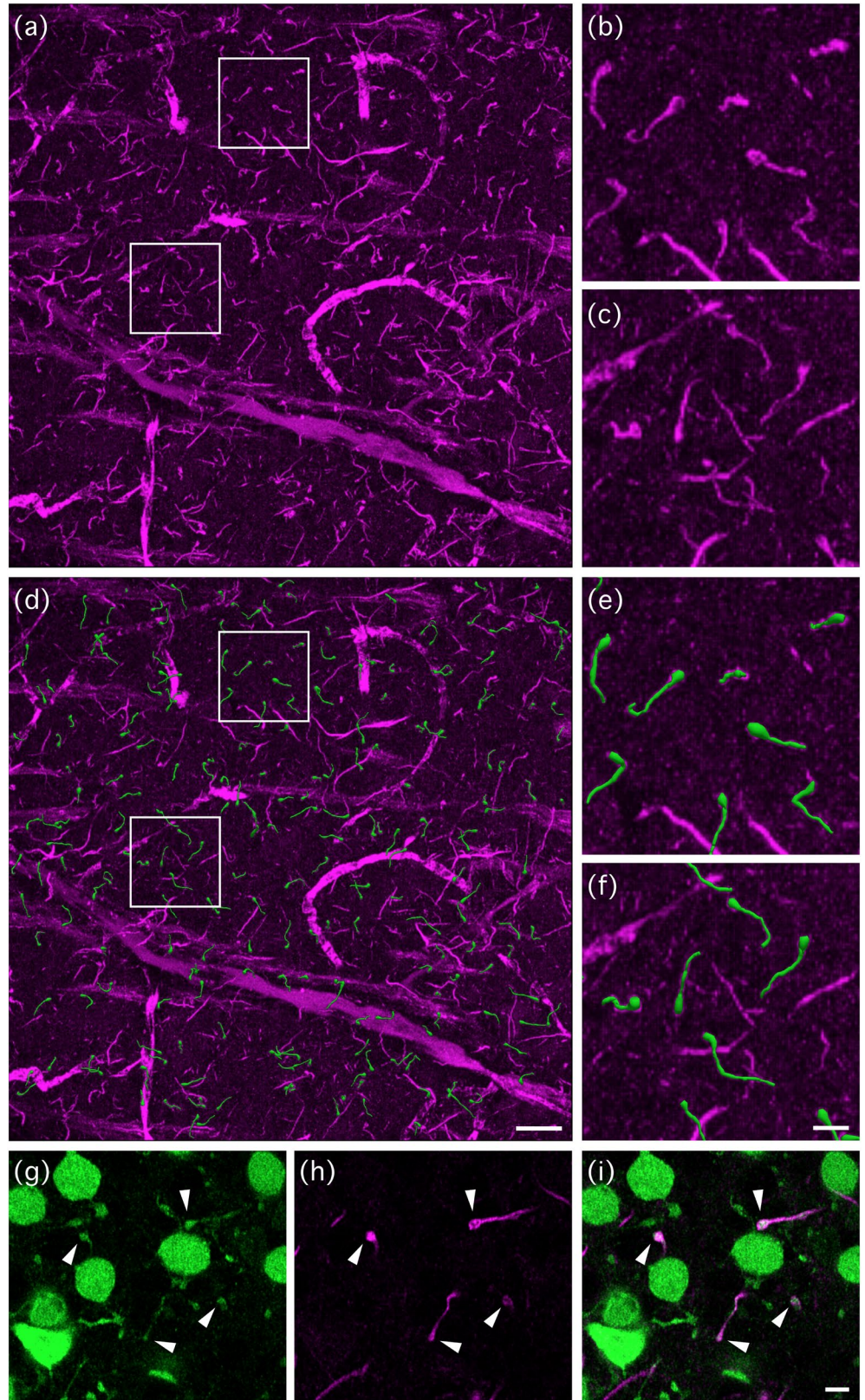


(nearest-neighbor distances) and Figure 11(i) (regularity indices). For a given retinal quadrant and eccentricity, the nearest-neighbor distance was lower and more variable for the ankyrin-G-labeled process endings than for the AII amacrine cell bodies (compare Figure 5(f) and Figure 11(h)), suggesting that the distribution of endings displays low regularity. This was confirmed by the regularity index, which was ~2
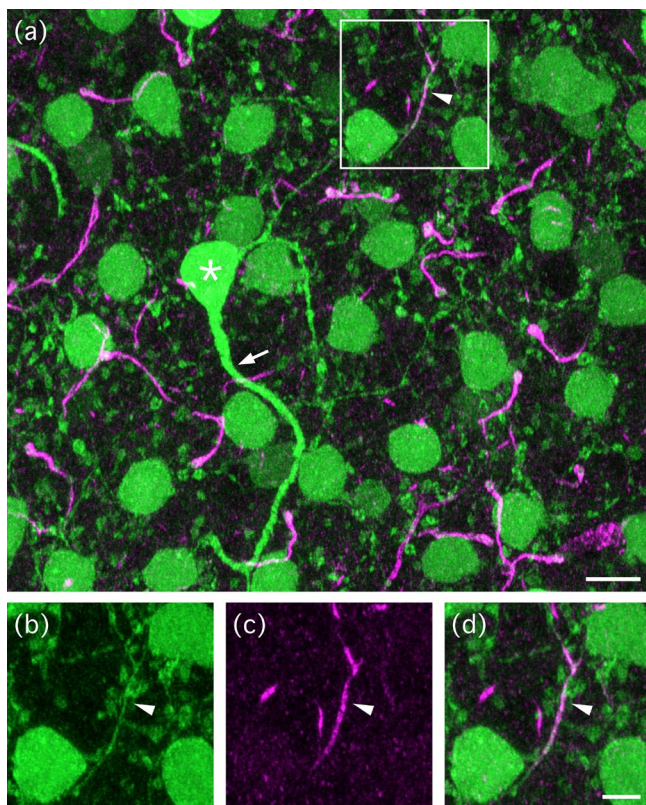
**FIGURE 8** Ankyrin-G expressed by processes of parvalbumin-labeled widefield amacrine cells. (a) Maximum intensity projection of slab (6.6 μm thick) of confocal image stack from wholemount immunolabeled for parvalbumin and ankyrin-G. The difference in intensity between AII and non-AII parvalbumin-labeled cell bodies is no longer apparent because the image was adjusted to enhance visualization of weakly labeled processes. The cell body marked by an asterisk belongs to a widefield amacrine cell. Notice how the cell body gives rise to both the thick process (marked by arrow) that travels horizontally for a considerable distance in the lower part of the image, as well as a thinner process that travels horizontally towards the upper, right half of the image and displays colocalization with ankyrin-G far from the cell body (marked by arrow head). The square region demarcated by white borders is displayed in (b-d). Notice several examples of colocalization between parvalbumin and ankyrin-G in AIS-like processes of AII amacrine cells. Scale bar, 10 μm. (b-d) Detailed view of ankyrin-G-labeled process of parvalbumin-labeled widefield amacrine cell (arrow heads in same relative position as in (a)). Each image displays a maximum intensity projection with labeling for parvalbumin (green, displayed separately in (b)) and immunolabeling for ankyrin-G (magenta, displayed separately in (c)), with overlay between parvalbumin and ankyrin-G signals in (d). Scale bar, 5 μm (b-d) [Color figure can be viewed at wileyonlinelibrary.com]

(2.02 ± .19; range 1.74–2.34; $n = 16$ stacks), markedly lower than for the AII cell bodies and with little dependence on location in the retina (Figure 11(i)). The corresponding results for the origins of the ankyrin-G-labeled processes were very similar (1.97 ± .15; range 1.66–2.18; $n = 16$ stacks; data not shown).

In addition to directly calculating the regularity index (Figure 11 (i)), we also analyzed the distributions of nearest-neighbor distances

for ankyrin-G-labeled process endings in more detail for the four most central (#4) and the four most peripheral regions (#1, Figure 12 (a); location illustrated in Figure 5(a)). As illustrated in Figure 12(b), (c), the histograms that displayed the corresponding frequency distributions were well fitted by the functions for the expected random distributions adjusted for the observed spatial densities. This strongly suggested that the ankyrin-G-labeled process endings were randomly distributed. The major reason for the difference between the AII cell bodies and the ankyrin-G-labeled process endings is that the much smaller size of the latter imposes less of a constraint on the spatial distribution and allows a random distribution to be observed.

## 3.4 | Laminar distribution of ankyrin-G-labeled processes of AII amacrine cells

The origin of the ankyrin-G-labeled processes of dye-injected AII amacrine cells was typically located in the distal part of the inner plexiform layer or in the proximal part of the inner nuclear layer (Figure 1). In contrast, there seemed to be considerably larger variation in the laminar distribution of the terminal part of the process. In wholemount retina, the ankyrin-G-labeled processes could be observed to travel locally in the immediate neighborhood close to the site of origin, or, alternatively, to travel for a considerable distance in either the inner nuclear or inner plexiform layer (Figure 13(a), (b)). For a quantitative analysis, we calculated the number of origins and endings and the total length of reconstructed AII-type ankyrin-G-labeled processes located in either the inner nuclear layer, the inner plexiform layer (individually for strata S1-S5), or the ganglion cell layer. As illustrated in Figure 13(c), the majority of origins were located in the inner nuclear layer and in S1-S3, with a peak in S1. In contrast, the endings were distributed across the inner nuclear and inner plexiform layers, with a gradient from the distal (higher density) to the proximal (lower density) retina (Figure 13(c)). The largest fraction of the length of ankyrin-G-labeled processes was located in the inner nuclear layer and in S1-S3, with a peak in S1 for the dorsal retina. For both origins, endings, and process length, there was little difference between retinal quadrants and eccentricities (Figure 13(c)).

## 3.5 | Orientation of ankyrin-G-labeled processes of AII amacrine cells

As illustrated in Figure 13(b), some of the ankyrin-G-labeled processes ascend toward and into the inner nuclear layer, whereas others descend deeper into the inner plexiform layer. It is not obvious, however, if there are preferential orientations or other differences between retinal regions or between central and peripheral retina. This has implications for the potential synaptic connectivity of the ankyrin-G-labeled processes of AII amacrine cells.

To examine this, we translated the relative positions of all reconstructed AII-type ankyrin-G-labeled processes within a single

**FIGURE 9** Comparison of morphological properties of ankyrin-G-labeled processes identified by immunolabeling of wholemount retina (AII- and non-AII-type) and of retinal slices with dye-injected AII amacrine cells. (a) Schematic figure of wholemount retina and the location of three high-resolution confocal image stacks used for counting and morphological analysis of AII- and non-AII-type ankyrin-G-labeled processes. (b) Scatter plots of the relationship between the maximum diameter of the distal 5 μm of the ankyrin-G-labeled segment and the average (length-weighted) diameter of the proximal 50% of the total length of the same segment. Blue points correspond to processes classified as AII-type based on a visually identified terminal swelling. Red points correspond to processes classified as non-AII-type based on the lack of a terminal swelling (at either end). The three scatter plots display data for the three regions indicated in (a). Notice the minimal overlap between data points for the two types of visually identified processes. (c) Combined scatter plot of all data points from the individual plots in (b), overlaid with data points for processes identified as AIS-like after immunolabeling retinal slices with dye-injected AII amacrine cells (as in Figure 1, same processes as in Figure 3(h), but from analysis after user-guided/semi-automatic reconstruction). Notice that the large majority of data points for AIS-like AII processes overlap with the data points for visually identified AII-type ankyrin-G-labeled processes in the retina wholemount [Color figure can be viewed at wileyonlinelibrary.com]
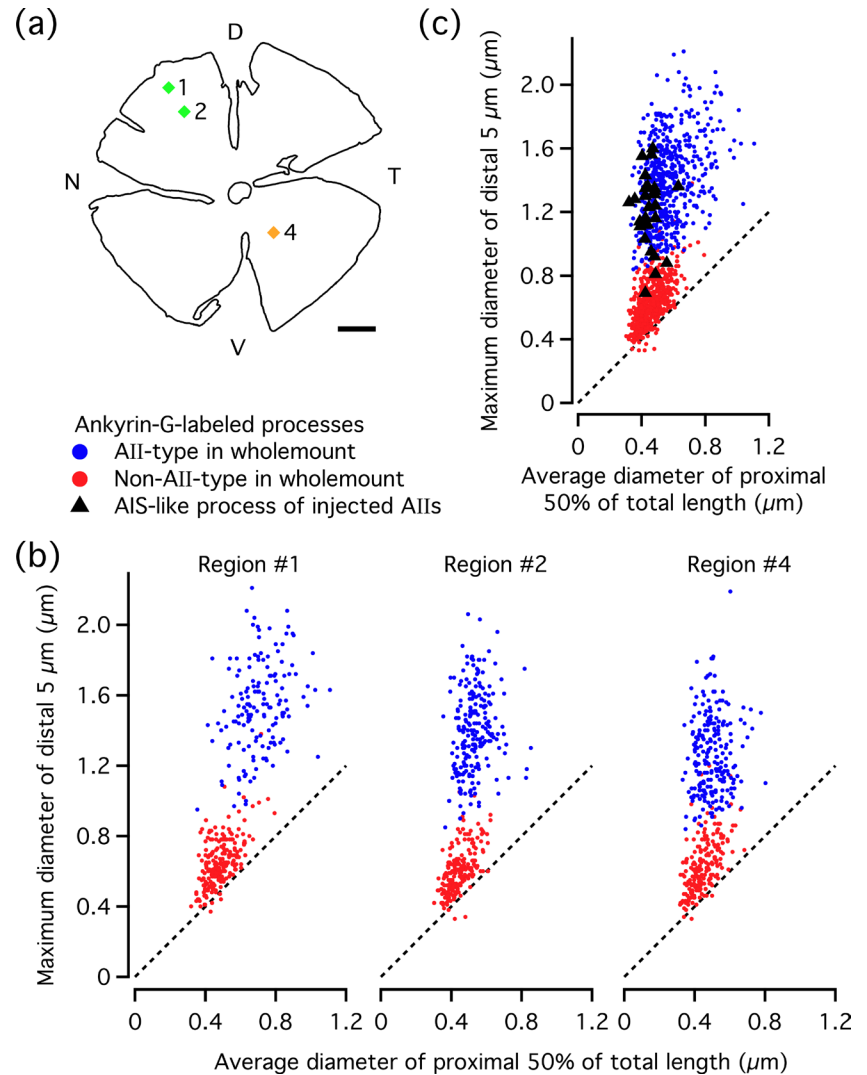


image stack such that the proximal ends of the processes started at a common origin. This is similar to the analysis performed by Boycott et al. (1978) for the orientation of the axon terminal system of Golgi-impregnated B-type horizontal cells in cat retina. The results from the four most central image stacks (#4) are displayed in Figure 14(a)-(d), with the translated processes projected both onto a horizontal plane parallel to the retinal surface (XY; Figure 14(a)-(d), top left) and onto a vertical plane (XZ; Figure 14(a)-(d), bottom left). From the horizontal plane projection, there seemed to be no preferential orientation. From the vertical plane projection, there seemed to be a preference for projections close to horizontal, with fewer processes following a more vertical orientation (ascending or descending). Because the variation in length of the ankyrin-G-labeled processes could mask short processes in the plots, we also displayed the distribution of the endings after normalizing the lengths of all processes (such that the endings would all be located on the surface of a sphere) and projecting the corresponding points onto a horizontal (XY; Figure 14 (a)-(d), top right) or a vertical plane (XZ; Figure 14(a)-(d), bottom right). When we graphed the results for the four most peripheral image

stacks (#1; Figure 14(e)-(h)), the results were very similar to those for the most central image stacks. For both central and peripheral regions, the displays of ending points confirmed the lack of preference in the horizontal plane and indicated a moderate preference for horizontal and descending orientations in the vertical plane.

## 3.6 | Spatial relation between the ankyrin-G-labeled processes and the dendritic fields of AII amacrine cells

If the ankyrin-G-labeled process of an AII amacrine cell is involved in synaptic relationships with processes from other retinal neurons, it is of interest to examine if it is confined to the dendritic fields defined in the horizontal plane by the ordinary lobular and arboreal dendritic processes of the AII. From dye-injected AII amacrines in slices, it sometimes appeared as if the ankyrin-G-labeled process extended markedly further in the horizontal direction than the other dendritic processes (e.g., Figure 1(b), see also Figure 14).
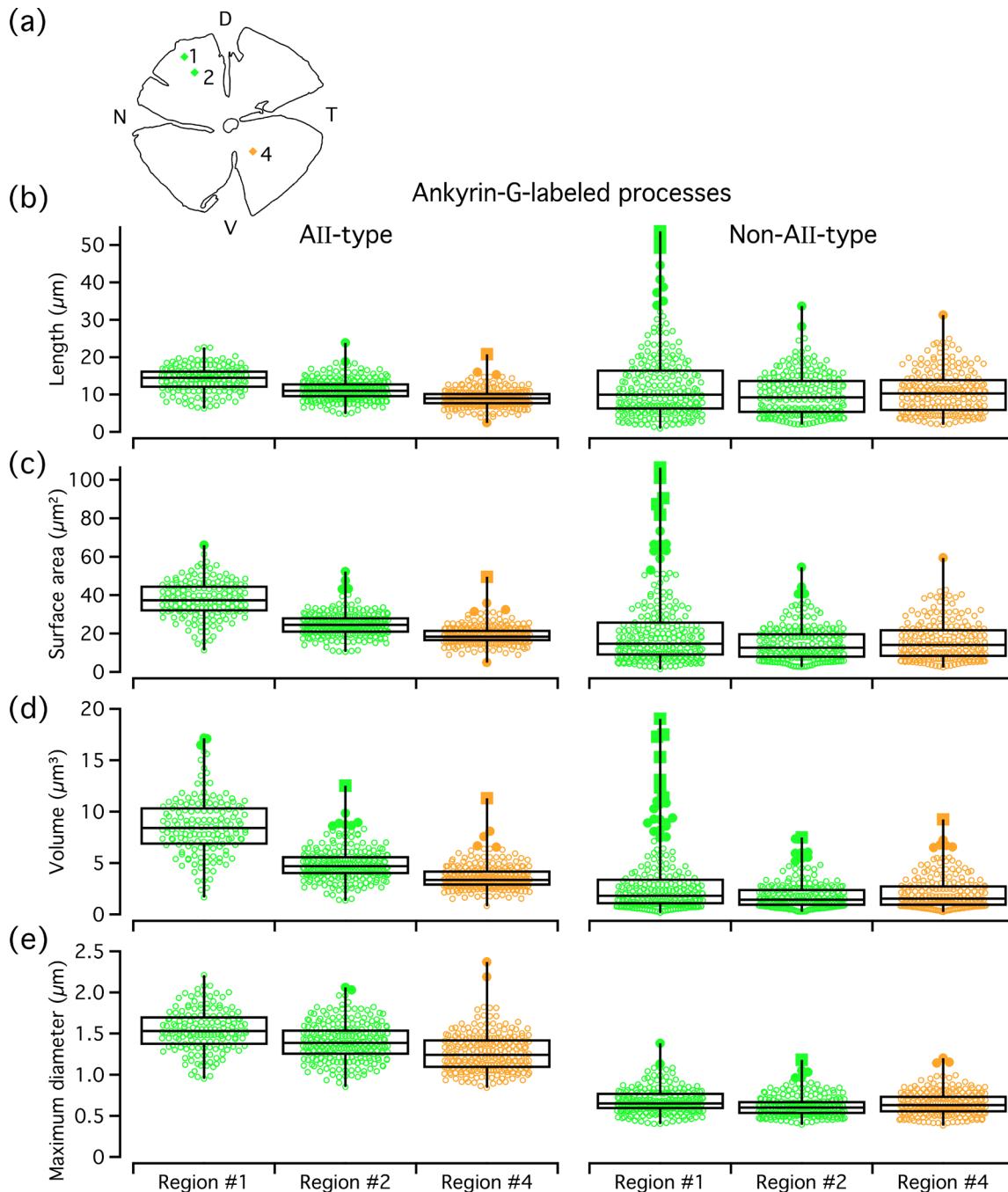
**FIGURE 10** Morphological properties of AII-type and non-AII-type ankyrin-G-labeled processes in retina wholemount (immunolabeled for ankyrin-G and parvalbumin). (a) Schematic figure of wholemount retina and the location of three high-resolution confocal image stacks used for morphological analysis. (b-e) Box and whisker scatter plots for length (b), surface area (c), volume (d), and maximum diameter (e) of AII-type (left column) and non-AII-type (right column) processes. The colors and region numbers correspond to those in the schematic figure in (a). Here and later, the horizontal line within each box corresponds to the median, the boxes themselves correspond to the interquartile range (IQR; difference between the 75th and 25th percentiles), and the whiskers indicate the total range for each region. Filled circles are outliers, defined as data points with value > [third quartile + (1.5 × IQR)] or value < [first quartile - (1.5 × IQR)]. Filled squares are far outliers, defined as data points with value > [third quartile + (3 × IQR)] or value < [first quartile - (3 × IQR)]. All properties quantified by analysis of morphological reconstructions of ankyrin-G-labeled processes [Color figure can be viewed at wileyonlinelibrary.com]

Systematically investigating the dendritic fields of a population of AII amacrine cells within a given region of the retina will ideally require complete visualization of all individual dendritic trees, which is currently not feasible. As a first approximation, however, we

calculated the Dirichlet domains from the information provided by the distribution of the segmented cell bodies of AII amacrine cells, identified by immunolabeling for parvalbumin (Figure 4). For some types of neurons that form a regular mosaic by tiling the retina (in the
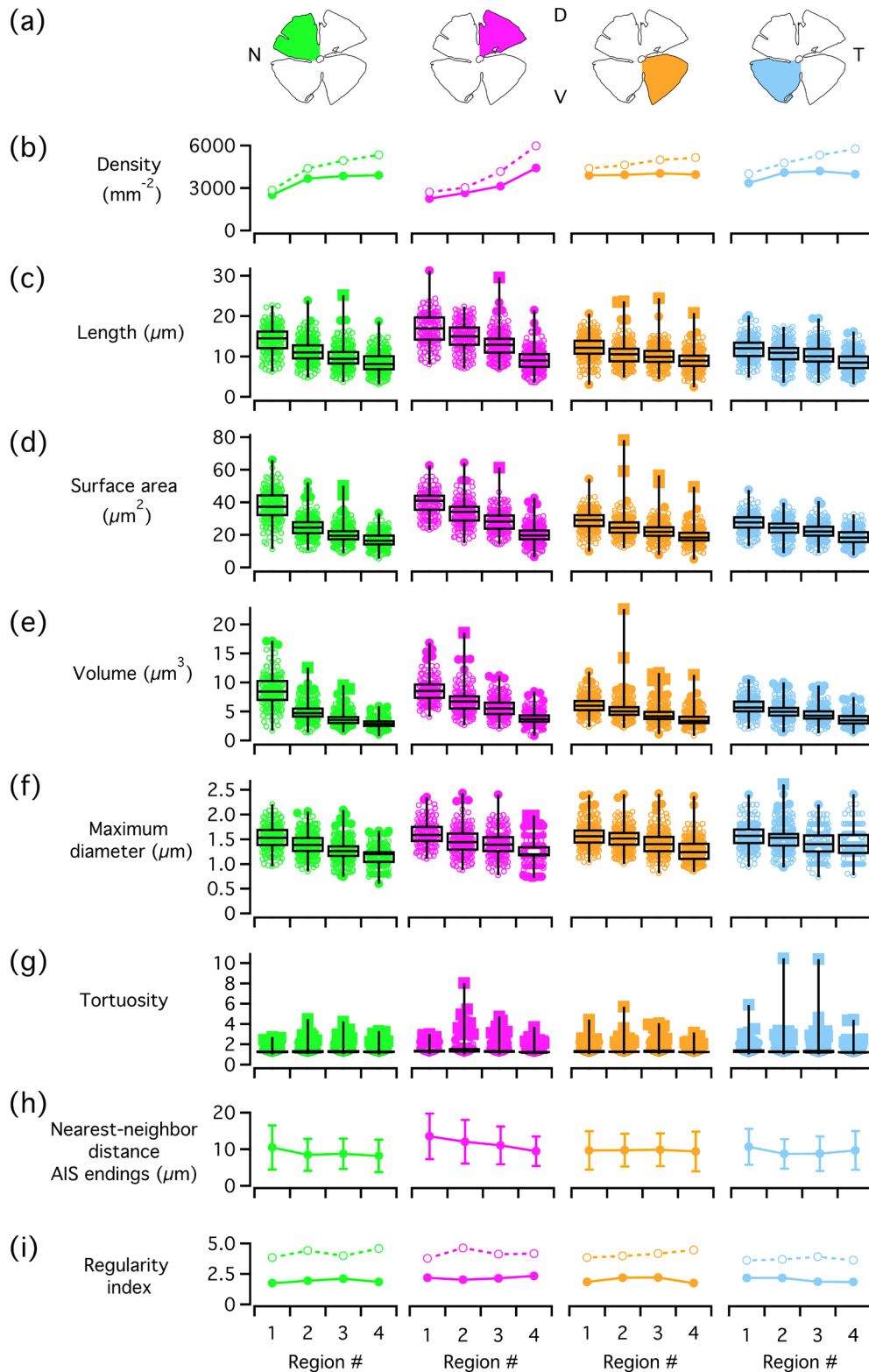
**FIGURE 11** Morphological properties of AII-type ankyrin-G-labeled processes as a function of retinal location (quadrant) and eccentricity (region number). (a) Schematic figures of wholemount retina. All 16 high-resolution confocal image stacks (as in Figure 5(a)) were used for morphological analysis. In all graphs (b-i), colors correspond to those of the quadrants in (a) and region numbers correspond to those in Figure 5(a). Box and whisker scatter plots as in Figure 10. All properties quantified by analysis of morphological reconstructions of ankyrin-G-labeled processes. (b) Spatial density of ankyrin-G-labeled processes (filled circles and continuous lines). For comparison, the corresponding data for AII cell bodies (same as in Figure 5(b)) have been overlaid (open circles and broken lines). (c) Anatomical (non-Euclidean) length. (d) Surface area. (e) Volume. (f) Maximum diameter. (g) Tortuosity. (h) Nearest-neighbor distance between the endings (distal tips) of ankyrin-G-labeled processes. (i) Regularity index for the distribution of the endings of ankyrin-G-labeled processes in the XY (horizontal) plane (filled circles and continuous lines). For comparison, the corresponding data for AII cell bodies (same as in Figure 5(h)) have been overlaid (open circles and broken lines) [Color figure can be viewed at wileyonlinelibrary.com]
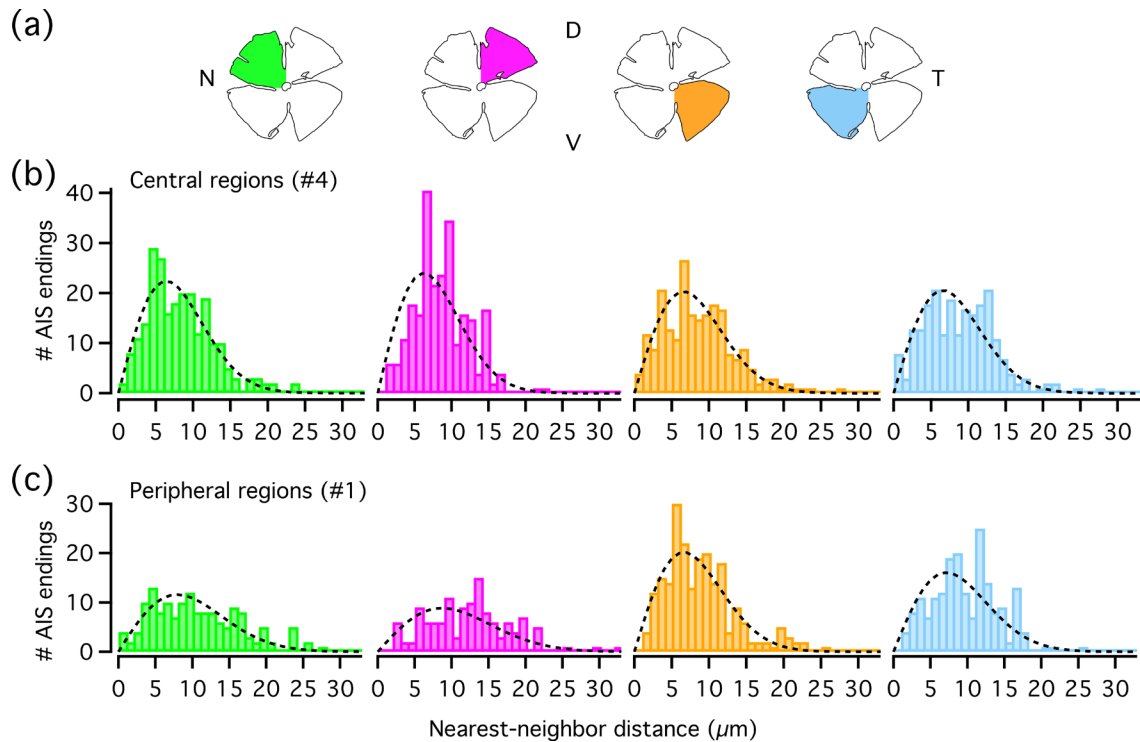
**FIGURE 12** Random distribution of nearest-neighbor distances for the endings (distal tips) of AII-type ankyrin-G-labeled processes. (a) Schematic figures of wholemount retina. In all graphs (b, c), colors correspond to those of the quadrants in (a) and region numbers correspond to those in Figure 5(a). (b) Frequency histograms displaying the distribution of nearest-neighbor distances for endings of AII-type ankyrin-G-labeled processes in the XY (horizontal) plane within the most central region (#4) in each retinal quadrant. The broken black line in each panel shows the expected probability density function (multiplied by the total number of cells for a given region; equation 5) for a randomly distributed population with the same spatial density (for details, see Materials and Methods). Notice the close correspondence between the histograms and the theoretical curves for random distributions. (c) As in (b), but for the most peripheral region (#1) in each retinal quadrant [Color figure can be viewed at wileyonlinelibrary.com]

horizontal plane), the Dirichlet domains correspond approximately to the dendritic fields, for example, ON-α-type retinal ganglion cells where the coverage factor is 1.4 (Wässle et al., 1981). For the lobular dendritic fields of rat AII amacrine cells, Wässle et al. (1993) reported a coverage factor of ~1, suggesting that the Dirichlet domains approximate the lobular dendritic fields. When we overlaid projections of the AII-type ankyrin-G-labeled processes on the Dirichlet domains, it was obvious that a large number of processes crossed the borders between neighboring domains (Figure 15). This was the case both for central (Figure 15(a)-(d)) and peripheral retina (Figure 15(e)-(h)).

For the arboreal dendritic fields of rat AII amacrine cells, Wässle et al. (1993) estimated a coverage factor of ~3. To mimic this situation, we digitally expanded the calculated Dirichlet domains for two of the image stacks in the dorsal temporal quadrant (Figure 16(a); one central, one peripheral) isotropically (keeping the positions of the centroids fixed) to achieve a coverage factor of 3 and used the expanded domains as an approximation for the arboreal dendritic fields. Because there was considerable overlap of the expanded Dirichlet domains, it was difficult to obtain a good impression of the relation between the domains and the (projections of the) ankyrin-G-labeled processes (Figure 16(b), (c)). To facilitate visual inspection, we removed a number of domains until there was no overlap. For the expanded domains

illustrated in Figure 16(d), (e), we observed several examples where at least one ankyrin-G-labeled process was fully enclosed within a domain. For a quantitative analysis, we counted the number of ankyrin-G-labeled processes that crossed a border between Dirichlet domains. This was done for both the original Dirichlet domains and after expansion to achieve a coverage factor of 3. For the original Dirichlet domains, the fraction of ankyrin-G-labeled processes that crossed domain borders was 63.1% ± 7.0% (range 50.5–74.5%, $n = 16$ regions). After expansion (coverage factor = 3), only 9.7% ± 3.5% (range 3.6%–14.7%, $n = 16$ regions) of the processes crossed domain borders. To the extent that the original and expanded Dirichlet domains are representative of the lobular and arboreal dendritic fields, respectively, these results suggest that the ankyrin-G-labeled process of an AII amacrine typically extends beyond the lobular, but not beyond the arboreal dendritic fields.

## 4 | DISCUSSION

The first explicit morphological identification of the AII as a specific type of mammalian amacrine cell was reported for cat retina by Kolb and Famiglietti (1974), with a more detailed morphological analysis
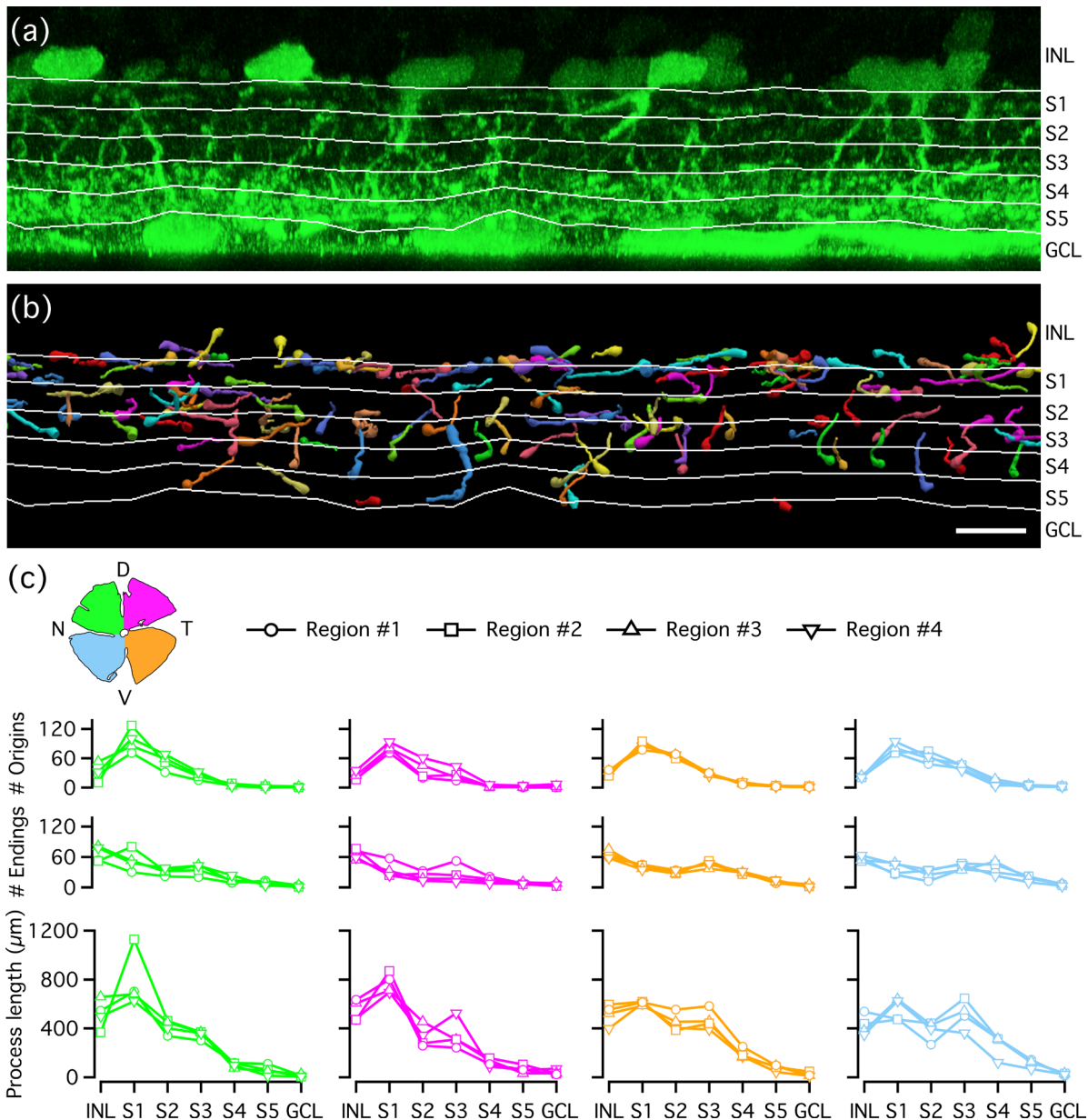
**FIGURE 13** Laminar distribution of AII-type ankyrin-G-labeled processes. (a) Maximum intensity projection (XZ) of vertical slab (9.9 μm thick) from high-resolution confocal stack in wholemount immunolabeled for ankyrin-G and parvalbumin, displaying immunolabeling for parvalbumin (green). Here and in (b), borders between retinal layers and between strata (S1-S5) of the inner plexiform layer are indicated by horizontal lines. The subdivisions of the inner plexiform layer were generated by manually delineating the borders towards the inner nuclear and ganglion cell layers, and dividing the vertical distance between the borders in five equidistant strata at regular intervals (for details, see Materials and Methods). (b) As in (a), but with projection of all morphologically reconstructed AII-type ankyrin-G-labeled processes of vertical slab (246.03 μm thick) from the same confocal image stack. Colors have been randomly assigned to different processes for improved visualization. Scale bar, 10 μm (a, b). (c) Laminar distribution of the number of origins (location 2 in Figure 1(i)) and endings (location 3 in Figure 1(i)) and the total length of AII-type ankyrin-G-labeled processes as a function of retinal quadrant and eccentricity. Inset shows a schematic figure of the wholemount retina where the color of each quadrant corresponds to the colors of the graphs. The region numbers correspond to those in Figure 5(a) (#1, circles; #2, squares; #3, triangles; #4, inverted triangles) [Color figure can be viewed at wileyonlinelibrary.com]

reported shortly after (Famiglietti & Kolb, 1975). The observation, almost 20 years later, of spiking mediated by Na$_v$ channels (in rat AIIs; Boos et al., 1993) immediately prompted the question of the functional importance of the spiking, as well as the subcellular location of the Na$_v$ channels and the mechanism of spike generation. However, this discovery did not lead to a revision of the earlier conclusion that

AII amacrines lack an axonal process (Famiglietti & Kolb, 1975; Kolb & Famiglietti, 1974; Vaney, 1985), in common with other types of amacrine cells (Cajal, 1892, 1894). In contrast, the studies of Wu et al. (2011) and Cembrowski et al. (2012) of mouse AIIs unequivocally demonstrated that a previously described "morphologically distinct process" with unknown cellular identity (van Wart et al., 2005) in fact
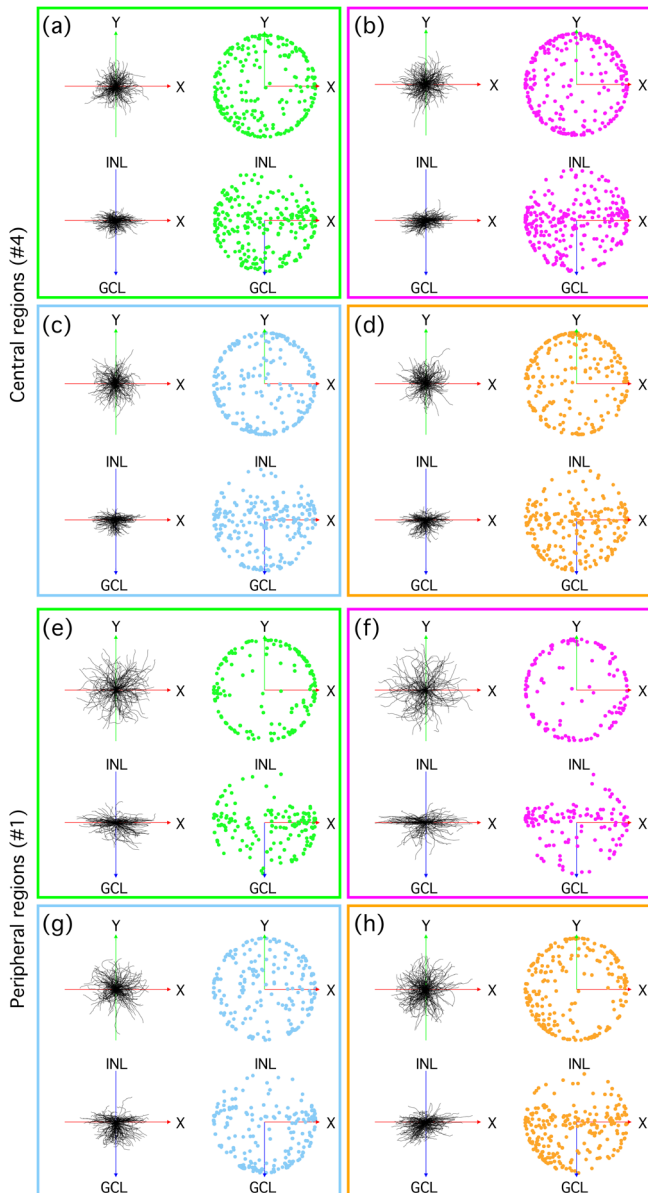
**FIGURE 14** Orientation of AII-type ankyrin-G-labeled processes in the horizontal (XY) and vertical (XZ) planes in central and peripheral regions of the retina. (a-d) Orientation of processes located in the four most central regions (#4 in Figure 5(a)). Here and in (e-h), the panel frame color is the same as the color of the corresponding confocal image stacks of each retinal quadrant in Figure 5(a). The figure in the upper left part of each panel was generated by projecting the reconstruction of each process onto the XY plane, followed by translation to locate the proximal end of each process at the origin of the coordinate system (XY). The figure in the upper right panel of each figure was generated in the same way, but after normalizing the Euclidean length of each process (straight-line distance from origin to ending) and only plotting the ending of each process (filled circle). The figures in the bottom of each panel were generated in the same way, but for projections in the XZ plane. The relative positions of the inner nuclear layer and ganglion cell layer as indicated. Axis length 40 μm (X, Y; −20 to +20 μm; (a-h)). (e-h) As for (a-d), but for the four most peripheral regions (#1 in Figure 5(a)) [Color figure can be viewed at wileyonlinelibrary.com]

belongs to the AII amacrine cell. This process displays molecular characteristics that identify it as an AIS-like process and is crucial for generating the action potentials. Once the AIS-like process was recognized as often displaying a characteristic appearance and orientation (e.g., Figure 1(a), (b)), it became possible to recognize its likely identity in earlier studies simply by the morphology (e.g., see Figure 12 in Hartveit, 1997 and Figure 6 in Veruki et al., 2010). As a unique structural element of the AII amacrine cell, the AIS-like process and the action potentials that it generates are likely to have an important functional role for the signal processing taking place in this cell. Although spiking mediated by $Na_v$ channels located at an AIS-like process is found in both rat and mouse AIIs, it is not known if these properties are common to AIIs of all mammalian retinas, including animals commonly used in studies of the retina (e.g., rabbit, cat, and primate). Here, we investigated the general morphological properties and identifying characteristics of rat AIIs to determine whether the orientation and location of the AIS-like process can provide clues to potential synaptic connectivity.

## 4.1 | General morphological properties of the AIS-like process of AII amacrines

With the goal of analyzing the morphological properties of the AIS-like process as a function of retinal eccentricity, we needed to first establish a set of morphological criteria that would allow us to identify all AII-type AIS-like processes as reliably as possible. Although AII amacrine cell bodies in rat can be immunolabeled for parvalbumin (Wässle et al., 1993), the labeling intensity of the complete dendritic tree is in general too low for robust identification across the retina. Instead, we used intracellular injection to fill AIIs in retinal slices with fluorescent dye and immunolabeling for ankyrin-G to identify the AIS-like process. Although the majority of injected cells displayed a process with ankyrin-G labeling, the fraction of cells where no such process could be identified was ~10% (5/48 cells). This is higher than expected from physiological work in our laboratory with whole-cell recording of AII amacrines in slices, where almost every cell displays TTX-sensitive, depolarization-evoked action currents or potentials (e.g., Mørkve et al., 2002). We do not know if every cell with physiological evidence for the presence of $Na_v$ channels would also display an ankyrin-G-labeled, AIS-like process, but the possibility should be considered that cell injection might compromise subsequent immunolabeling (e.g., Dedek et al., 2006; Wässle et al., 1993).

From the morphological analysis of dye-injected and immunolabeled AII amacrines, we analyzed a series of morphological properties that served as a basis for the subsequent identification of AII-type AIS-like processes in retinal wholemounts immunolabeled for ankyrin-G. The segment with ankyrin-G labeling is very distinct, with an abrupt transition from the unlabeled region at the proximal end. The length of the labeled segment can vary considerably, ranging from ~2 to almost 20 μm in our material. At the distal end, the labeling for ankyrin-G extends almost to the distal tip, typically with a short unlabeled region (≤1 μm). A consistent morphological

## Central regions (#4)



## Peripheral regions (#1)
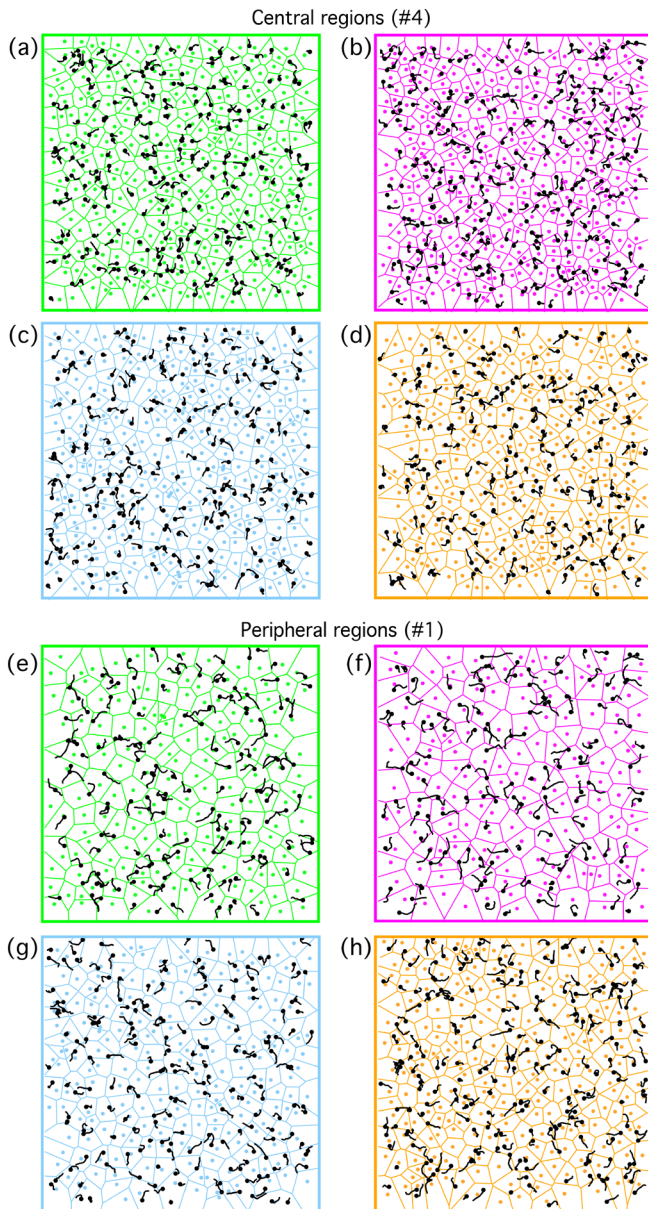
**FIGURE 15** Location of AII-type ankyrin-G-labeled processes relative to Dirichlet domains estimated from distribution of AII amacrine cell bodies. (a-d) Location of processes in the four most central regions (#4 in Figure 5(a)). Here and in (e-h), the color of the panel frame is the same as the color of the corresponding confocal image stacks in each retinal quadrant in Figure 5(a). For each panel, the Dirichlet domains (drawn by thinner lines) were calculated from the center-of-mass coordinates (centroids) in the XY (horizontal) plane, marked by colored circles of the AII amacrine cell bodies (identified by immunolabeling for parvalbumin). The projection (in the XY plane) of each AII-type ankyrin-G-labeled process is drawn by a black line, with the location of the terminal swelling marked by a black circle. The size of each panel frame corresponds to the XY size of the confocal image stack ($246.03 \times 246.03 \ \mu m^2$). (e-h) As for (a-d), but for the four most peripheral regions (#1 in Figure 5(a)) [Color figure can be viewed at wileyonlinelibrary.com]

feature is the presence of a terminal swelling, typically two- to fourfold thicker than the average diameter at the proximal end. We did notice, however, that in a few cases the labeling did not

extend to the very distal tip of the process such that no terminal swelling was visible.

## 4.2 | Identification of AII-type AIS-like processes in the retina

Although the number of ankyrin-G-labeled processes identified as AII-type was consistently (slightly) lower than the number of AII-type parvalbumin-labeled cell bodies, it is not possible that all ankyrin-G-labeled processes (in the inner plexiform layer) belong to AII amacrine cells, as the number is simply too high. We consider the most likely and important explanation for the relatively small discrepancy (between the number of AII-type AIS-like processes and the number of AII cells), to be the lack of a terminal swelling in some ankyrin-G-labeled segments of AIIs. This is expected from the experiments with dye-filled AIIs in retinal slices and will give rise to a small proportion of false negatives.

Based on previous work, it is likely that some non-AII-type ankyrin-G-labeled processes in the inner nuclear and inner plexiform layers could correspond to ankyrin-G-labeled axon segments of specific types of cone bipolar cells that express $Na_v$ channels (Cui & Pan, 2008; Hellmer et al., 2016; Vielma & Schmachtenberg, 2016), similar to the DB3a and DB4 cone bipolar cells in primate retina (Puthussery et al., 2013). In addition, we observed that some of the non-AII amacrine cells immunolabeled for parvalbumin displayed an ankyrin-G-labeled process. None of the processes identified in this way displayed a bulb or swelling at either end. The AISs of retinal ganglion cells are also labeled for ankyrin-G, but the lack of a terminal swelling and the location in the nerve fiber layer, as opposed to the inner plexiform layer, make their differentiation from AII-type processes straightforward.

## 4.3 | Distribution of AII amacrine cells and AII-type AIS-like processes across the retina

An important goal of this study was to analyze the distribution and orientation of the AII-type AIS-like processes. First, we found that they do not display any preferred orientation in the horizontal plane. In the vertical plane, the AIS-like processes display an overall preference for a horizontal orientation, but can also been seen to ascend towards and into the inner nuclear layer or to descend towards the proximal inner plexiform layer. Whereas the distribution of AII amacrine cell bodies appeared regular, with a nearest-neighbor distance regularity index of ~4 and corresponding histograms that could be well fitted by a Gaussian function, the distal endings of the AII-type AIS-like processes displayed a random distribution (cf. Wässle & Riemann, 1978). Although the apparently regular distribution of AII cell bodies in mouse retina could not be distinguished from a random distribution when cell body size was taken into account (cf. Keeley et al., 2020; Keeley & Reese, 2018), this difficulty of interpretation does not apply to the distribution of AII-type AIS-like process endings because of their considerably smaller size.
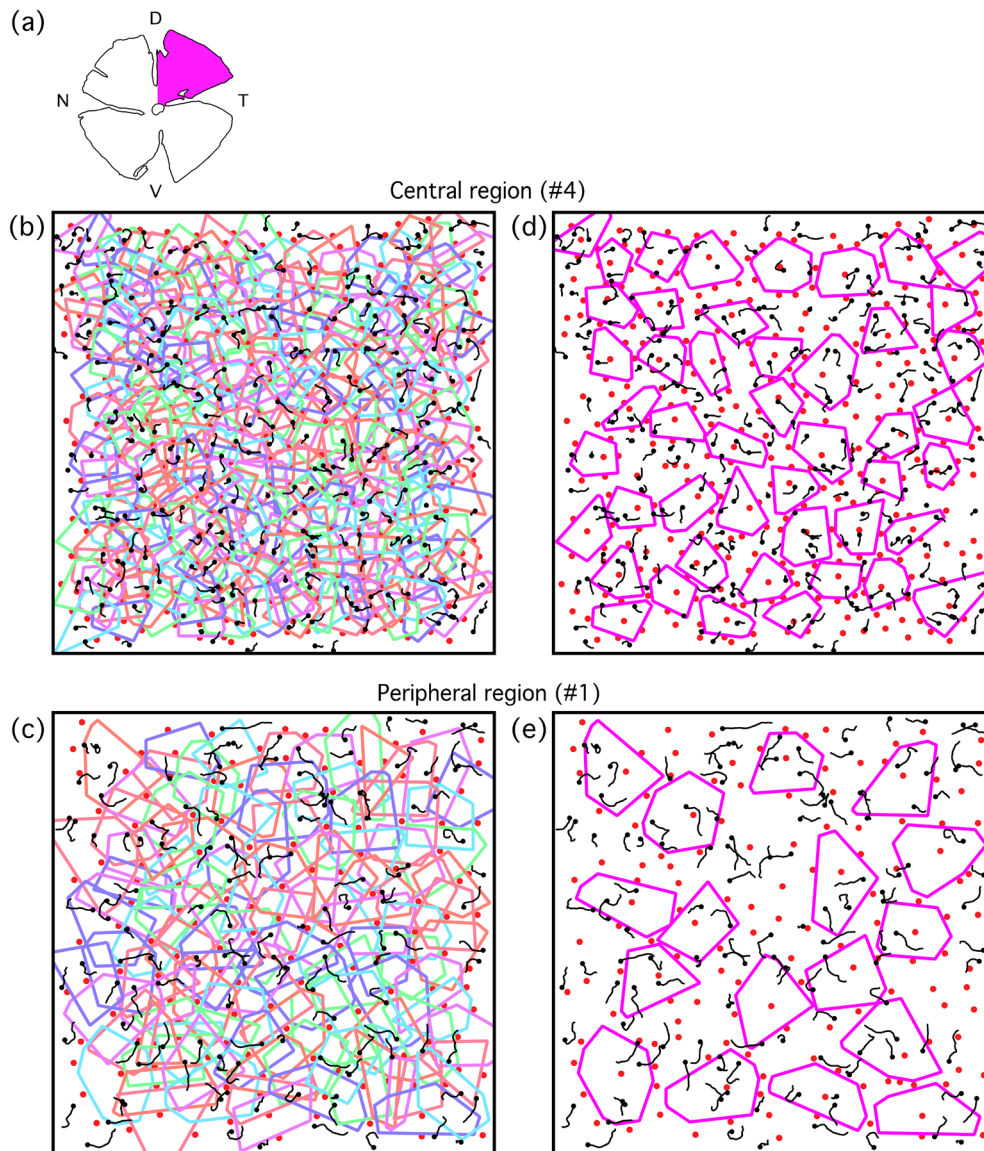
**FIGURE 16** Location of AII-type ankyrin-G-labeled processes relative to putative arboreal dendritic fields of AII amacrine cells. (a) Schematic figure of wholemount retina with location of analyzed image stacks indicated by colored quadrant (magenta). Putative arboreal dendritic fields were calculated from the Dirichlet domains (same as in Figure 15(b), (f), but only for domains fully enclosed within the borders of the confocal stack) by expanding them isotropically to achieve a coverage factor of 3 (see main text for details). (b, c) Putative arboreal dendritic fields (expanded Dirichlet domains) in the most central (#4) and most peripheral (#1) confocal image stacks (numbering as in Figure 5(a)). Colors have been randomly assigned to different fields for improved visualization. (d, e) Because extensive overlap of estimated dendritic fields in (b) and (c) made visualization difficult, we randomly selected a number of non-overlapping fields for display (#4 in (d); #1 in (e)). As in Figure 15, the locations of the centroids (center-of-mass coordinates) of the AII cell bodies are marked by colored circles and the projection (in the XY plane) of each AII-type ankyrin-G-labeled process is drawn by a black line, with the location of the terminal swelling marked by a black circle. The size of each panel frame corresponds to the XY size of the confocal image stack ($246.03 \times 246.03 \ \mu m^2$) [Color figure can be viewed at wileyonlinelibrary.com]

Our estimates for the distribution of AII amacrine cell bodies, including spatial density, nearest-neighbor distance and regularity index, are similar to those previously reported by Wässle et al. (1993). The peak density observed in our study ($\sim$5200 cells/mm$^2$) is somewhat lower than the peak densities reported by Wässle et al. (1993) for two retinas analyzed (7000 and 7500 cells/mm$^2$, respectively). The difference could be due to the exact locations sampled, potential

differences in the extent of shrinkage, and a (small) difference in age (e.g., from 3 weeks to 2 months postnatal, the retinal area increases from $\sim$40 to $\sim$50 mm$^2$; Nadal-Nicolás et al., 2018). Importantly, whereas the spatial density varies as a function of retinal eccentricity, with reduced density at more peripheral locations, the number of nearest neighbors and the regularity index both remain essentially constant across the retina. We also confirmed the finding of Wässle

et al. (1993) that immunolabeling for parvalbumin in addition to labeling AII cell bodies (and major processes) also labels the cell bodies of a second population of amacrine cells, most likely a type of widefield amacrine cell. As reported by Wässle et al. (1993), these cells can be easily separated from the population of AII amacrine cells by the higher intensity of labeling and the orientation and directional course of the primary dendrites.

## 4.4 | Potential synaptic connectivity of the AIS-like process of AII amacrine cells

According to our current understanding, action potentials of an AII amacrine cell are generated at the AIS-like process and spread passively to the rest of the cell (Cembrowski et al., 2012). From a given AII, action potentials can also spread passively across gap junctions functioning as electrical synapses, both between AII amacrine cells and between AII amacrine cells and ON-cone bipolar cells (Veruki & Hartveit, 2002a, 2002b). Both within a single cell and between cells, the propagation is subject to marked attenuation, as $Na_v$ channels have not been found in other locations than the AIS-like process (Cembrowski et al., 2012; Veruki & Hartveit, 2002a, 2002b; Wu et al., 2011).

It is currently not clear to which extent the functional importance of an action potential generated at the AIS-like process is linked to strong, but transient depolarization at the AIS-like process itself, or if it is related to the weaker, but longer-lasting depolarization reached after passive propagation to the rest of the cell (or both). If the AIS-like process is targeted by synaptic input, the presynaptic terminal(s) would be strategically positioned to exert a strong influence on the electrogenesis of the AII. This would be the case for both excitatory input (from axon terminals of bipolar cells) and inhibitory input (from other amacrine cells). Importantly, there is extensive evidence from other regions of the CNS for a specific type of axo-axonal synapse where an AIS is postsynaptic to terminals of an inhibitory neuron. Particularly well-studied examples are the *pinceau* synapses made by basket cell axons onto the AIS of Purkinje cells in the cerebellar cortex (Palay & Chan-Palay, 1974; Somogyi & Hámori, 1976) and by chandelier cell axons onto the AIS of pyramidal cells in the neocortex and hippocampus (Peters et al., 1968; Somogyi, 1977; Westrum, 1966). Although the pinceau complex of Purkinje cells seems to depend strongly on ephaptic transmission and to a much smaller extent on chemical (GABAergic) transmission, the synaptic organization mediates inhibition at the strategically important point of action potential initiation (Blot & Barbour, 2014).

Alternatively, or additionally, the AIS-like process could be presynaptic at a chemical synapse and release glycine, similar to ordinary AII lobular dendrites and appendages (Pourcho & Goebel, 1985). The computational modeling of Cembrowski et al. (2012) suggested that the AII action potential has a large amplitude and fast time course at the site of generation in the AIS-like process, quite different from the low amplitude and slow time course measured after passive propagation to the rest of the cell, including the cell body. Because of the difference in time course, the release characteristics for the AIS-like process could be considerably more transient than the sustained release thought to take place from the ordinary lobular appendages (Balakrishnan et al., 2015).

Our results would seem to cast doubt on the hypothesis that the AII amacrine AIS-like process is involved in synaptic relationships of the kind discussed above. A consistent finding is that synaptic connectivity in the inner plexiform layer of the retina is a function of stratification (reviewed by Masland, 2004). The classical example is the maintenance of ON- versus OFF-center visual responses, which, after generation at the synaptic connections between photoreceptors and bipolar cells in the outer plexiform layer, are forwarded via sign-conserving synaptic connections between bipolar cells and ganglion cells in the inner plexiform layer (for review, see Dowling, 2012; Euler et al., 2014). The morphological correlate is the co-stratification of bipolar cell axon terminals and ganglion cell dendrites, in the distal part of the inner plexiform layer for OFF-center responses and in the proximal part of the inner plexiform layer for ON-center responses. Similar observations have been made for other retinal microcircuits, such as the synaptic relationships between dendritic arbors of starburst amacrine cells, involved in generating direction selectivity, and the dendrites of different types of direction-selective ganglion cells (Briggman et al., 2011). In contrast, however, the AIS-like processes of AII amacrines display a surprising variability with respect to stratification level, orientation and distribution. Any pre- and/or postsynaptic partners of the AIS-like processes must themselves have processes across a correspondingly wide region. Specific types of bipolar cells or narrowly stratifying types of amacrine cells are unlikely candidates for a synaptic partnership. In contrast, diffusely stratifying amacrine cells could take part in synaptic relationships involving different locations of a dendritic arbor, but this hypothesis is difficult to reconcile with the substantial number of AIS-like processes that extend into the inner nuclear layer.

Earlier studies of the molecular specificity (Cembrowski et al., 2012; van Wart et al., 2005; Wu et al., 2011) and the presumed ultrastructure (Tsukamoto & Omi, 2013) of the AIS-like process do not seem able to provide definitive answers to these questions. The study of Tsukamoto and Omi (2013), with electron microscopic reconstruction of three AII amacrine cells from mouse retina, aimed at identifying the AIS-like process by applying ultrastructural criteria developed from general properties of the AIS in other types of neurons, for example, the presence of a dense undercoating along the plasma membrane (reviewed by Peters et al., 1991). Tsukamoto and Omi (2013) suggested that the AIS-like processes, identified by these criteria, could be postsynaptic at ribbon synapses from rod bipolar cells, postsynaptic at conventional synapses from amacrine cells and presynaptic at synapses onto unidentified neurons. A later study of AII amacrine cells in rabbit retina (Marc et al., 2014) found membrane densities similar to those described by Tsukamoto and Omi (2013), but could not verify that they were restricted to any specific process or subcellular compartment. For AII amacrine cells in rat and mouse retina, van Wart et al. (2005) and Wu et al. (2011) performed immunolabeling for several proteins with functions relevant for

synaptic transmission, including synaptic vesicle proteins (synaptophysin, synaptoporin) and the glycine receptor α1 subunit. However, because of the limited resolution of light microscopy, it was not possible to decide unequivocally whether any given labeling was genuinely localized to a given cellular process.

## 4.5 | Final comments

Although we cannot exclude that the AII amacrine AIS-like process takes part in conventional synaptic connections, we believe that the results obtained in the current study suggest that other modes of operation should be considered. For example, the structural and molecular properties of the AIS-like process could enable it to respond to volume neurotransmission by means of extrasynaptic receptors, either for neurotransmitters released at morphologically specialized synapses elsewhere in the neuropil (e.g., glutamate and GABA) or for neurotransmitters released from presynaptic terminals that often occur without closely apposed postsynaptic targets (e.g., dopamine). Although the lack of a consistent morphological localization and stratification for the AII amacrine AIS-like process is consistent with this scenario, more work is needed to clarify the molecular properties, potential synaptic connectivity, and functional role of this unique process.

### CONFLICT OF INTEREST

The authors declare that there is no conflict of interest.

### AUTHOR CONTRIBUTIONS

Jian Hao Liu performed cell injections, immunocytochemical labeling, confocal imaging, image analysis, and made the figures. Jeet Bahadur Singh performed cell injections, immunocytochemical labeling, and confocal imaging. Espen Hartveit and Margaret Lin Veruki performed image analysis, conceived and designed experiments, supervised the project, interpreted data, and wrote the manuscript. All authors commented on and approved the final version of the manuscript.

### PEER REVIEW

The peer review history for this article is available at https://publons.com/publon/10.1002/cne.25210.

### DATA AVAILABILITY STATEMENT

Raw data will be made available to researchers interested in them upon reasonable request, in accordance with journal policy.

### ORCID

*Jian Hao Liu* https://orcid.org/0000-0001-6500-2144

*Jeet Bahadur Singh* https://orcid.org/0000-0003-1738-2060

*Margaret Lin Veruki* https://orcid.org/0000-0002-0532-144X

*Espen Hartveit* https://orcid.org/0000-0003-1798-1901

### REFERENCES

Balakrishnan, V., Puthussery, T., Kim, M.-H., Taylor, W. R., & von Gersdorff, H. (2015). Synaptic vesicle exocytosis at the dendritic lobules of an inhibitory interneuron in the mammalian retina. *Neuron, 87*, 563–575.

Blot, A., & Barbour, B. (2014). Ultra-rapid axon-axon ephaptic inhibition of cerebellar Purkinje cells by the pinceau. *Nature Neuroscience, 17*, 289–295.

Boos, R., Schneider, H., & Wässle, H. (1993). Voltage- and transmitter-gated currents of AII-amacrine cells in a slice preparation of the rat retina. *Journal of Neuroscience, 13*, 2874–2888.

Borowska, J., Trenholm, S., & Awatramani, G. B. (2011). An intrinsic neural oscillator in the degenerating mouse retina. *Journal of Neuroscience, 31*, 5000–5012.

Boycott, B. B., Peichl, L., & Wässle, H. (1978). Morphological types of horizontal cells in the retina of the domestic cat. *Proceedings of the Royal Society of London B, 203*, 229–245.

Briggman, K. L., Helmstaedter, M., & Denk, W. (2011). Wiring specificity in the direction-selectivity circuit of the retina. *Nature, 471*, 183–188.

Cajal, S. R. y (1892). La rétine des vertébrés. *La Cellule, 9*, 119–257. English translation in *The Structure of the Retina* (1972), compiled and translated by S. A. Thorpe & M. Glickstein. Springfield, IL: Charles C. Thomas.

Cajal, S. R. y (1894). *Les Nouvelles Idées sur la Structure du Système Nerveux chez l'Homme et chez les Vertébrés*. Reinwald & Cie. English translation in *New Ideas on the Structure of the Nervous System in Man and Vertebrates* (1990), translated by N. Swanson & L. W. Swanson. Cambridge, MA: MIT Press.

Cembrowski, M. S., Logan, S. M., Tian, M., Jia, L., Li, W., Kath, W. L., Riecke, H., & Singer, J. H. (2012). The mechanisms of repetitive spike generation in an axonless retinal interneuron. *Cell Reports, 1*, 155–166.

Choi, H., Zhang, L., Cembrowski, M. S., Sabottke, C. F., Markowitz, A. L., Butts, D. A., Kath, W. L., Singer, J. H., & Riecke, H. (2014). Intrinsic bursting of AII amacrine cells underlies oscillations in the rd1 mouse retina. *Journal of Neurophysiology, 112*, 1491–1504.

Cook, P. B., & Werblin, F. S. (1994). Spike initiation and propagation in wide field transient amacrine cells of the salamander retina. *Journal of Neuroscience, 14*, 3852–3861.

Cui, J., & Pan, Z.-H. (2008). Two types of cone bipolar cells express voltage-gated $Na^+$ channels in the rat retina. *Visual Neuroscience, 25*, 635–645.

Dacey, D. M. (1989). Axon-bearing amacrine cells of the macaque monkey retina. *Journal of Comparative Neurology, 284*, 275–293.

Dacheux, R. F., & Raviola, E. (1986). The rod pathway in the rabbit retina: A depolarizing bipolar and amacrine cell. *Journal of Neuroscience, 6*, 331–345.

Dedek, K., Schultz, K., Pieper, M., Dirks, P., Maxeiner, S., Willecke, K., Weiler, R., & Janssen-Bienhold, U. (2006). Localization of heterotypic gap junctions composed of connexin45 and connexin36 in the rod pathway of the mouse retina. *European Journal of Neuroscience, 24*, 1675–1686.

Demb, J. B., & Singer, J. H. (2012). Intrinsic properties and functional circuitry of the AII amacrine cell. *Visual Neuroscience, 29*, 51–60.

Dowling, J. E. (2012). *The retina, an approachable part of the brain* (2nd ed.). Belknap Press of Harvard University Press.

Euler, T., Haverkamp, S., Schubert, T., & Baden, T. (2014). Retinal bipolar cells: Elementary building blocks of vision. *Nature Reviews Neuroscience, 15*, 507–519.

Famiglietti, E. V. (1992a). Polyaxonal amacrine cells of rabbit retina: Morphology and stratification of PA1 cells. *Journal of Comparative Neurology*, *316*, 391–405.

Famiglietti, E. V. (1992b). Polyaxonal amacrine cells of rabbit retina: PA2, PA3, and PA4 cells. Light and electron microscopic studies with a functional interpretation. *Journal of Comparative Neurology*, *316*, 422–446.

Famiglietti, E. V., Kaneko, A., & Tachibana, M. (1977). Neuronal architecture of on and off pathways to ganglion cells in carp retina. *Science*, *198*, 1267–1269.

Famiglietti, E. V., & Kolb, H. (1975). A bistratified amacrine cell and synaptic circuitry in the inner plexiform layer of the retina. *Brain Research*, *84*, 293–300.

Famiglietti, E. V., & Kolb, H. (1976). Structural basis for ON- and OFF-center responses in retinal ganglion cells. *Science*, *194*, 193–195.

Greschner, M., Field, G. D., Li, P. H., Schiff, M. L., Gauthier, J. L., Ahn, D., Sher, A., Litke, A. M., & Chichilnisky, E. J. (2014). A polyaxonal amacrine cell population in the primate retina. *Journal of Neuroscience*, *34*, 3597–3606.

Hartveit, E. (1996). Membrane currents evoked by ionotropic glutamate receptor agonists in rod bipolar cells in the rat retinal slice preparation. *Journal of Neurophysiology*, *76*, 401–422.

Hartveit, E. (1997). Functional organization of cone bipolar cells in the rat retina. *Journal of Neurophysiology*, *77*, 1716–1730.

Heintzmann, R. (2006). Band limit and appropriate sampling in microscopy. In J. E. Celis (Ed.), *Cell biology. A laboratory handbook* (Vol. 3, pp. 29–36). Elsevier.

Hellmer, C. B., Zhou, Y., Fyk-Kolodziej, B., Hu, Z., & Ichinose, T. (2016). Morphological and physiological analysis of type-5 and other bipolar cells in the mouse retina. *Neuroscience*, *315*, 246–258.

Kaneko, Y., & Watanabe, S.-I. (2007). Expression of $Na_v1.1$ in rat retinal AII amacrine cells. *Neuroscience Letters*, *424*, 83–88.

Keeley, P. W., Eglen, S. J., & Reese, B. E. (2020). From random to regular: Variation in the patterning of retinal mosaics. *Journal of Comparative Neurology*, *528*, 2135–2160.

Keeley, P. W., & Reese, B. E. (2018). The somal patterning of the AII amacrine cell mosaic in the mouse retina is indistinguishable from random simulations matched for density and constrained by soma size. *Visual Neuroscience*, *35*, e003.

Kolb, H., & Famiglietti, E. V. (1974). Rod and cone pathways in the inner plexiform layer of cat retina. *Science*, *186*, 47–49.

Kolb, H., Nelson, R., & Mariani, A. (1981). Amacrine cells, bipolar cells and ganglion cells of the cat retina: A Golgi study. *Vision Research*, *21*, 1081–1114.

Kordeli, E., Lambert, S., & Bennett, V. (1995). Ankyrin G. A new ankyrin gene with neural-specific isoforms localized at the axonal initial segment and node of Ranvier. *Journal of Biological Chemistry*, *270*, 2352–2359.

Leterrier, C. (2018). The axon initial segment: An updated viewpoint. *Journal of Neuroscience*, *38*, 2135–2145.

Marc, R. E., Anderson, J. R., Jones, B. W., Sigulinsky, C. L., & Lauritzen, J. S. (2014). The AII amacrine cell connectome: A dense network hub. *Frontiers in Neural Circuits*, *8*, 104. https://doi.org/10.3389/fncir.2014.00104

Masland, R. H. (2004). Neuronal cell types. *Current Biology*, *14*, R497–R500.

Masland, R. H. (2012). The neuronal organization of the retina. *Neuron*, *76*, 266–280.

Miller, R. F., & Dacheux, R. (1976). Dendritic and somatic spikes in mudpuppy amacrine cells: Identification and TTX sensitivity. *Brain Research*, *104*, 157–162.

Mørkve, S. H., Veruki, M. L., & Hartveit, E. (2002). Functional characteristics of non-NMDA-type ionotropic glutamate receptor channels in AII amacrine cells in rat retina. *Journal of Physiology*, *542*, 147–165.

Nadal-Nicolás, F. M., Vidal-Sanz, M., & Agudo-Barriuso, M. (2018). The aging rat retina: From function to anatomy. *Neurobiology of Aging*, *61*, 146–168.

Nelson, R. (1982). AII amacrine cells quicken time course of rod signals in the cat retina. *Journal of Neurophysiology*, *47*, 928–947.

Nelson, R., Famiglietti, E. V., & Kolb, H. (1978). Intracellular staining reveals different levels of stratification for on- and off-center ganglion cells in cat retina. *Journal of Neurophysiology*, *41*, 472–483.

Palay, S. L., & Chan-Palay, V. (1974). *Cerebellar cortex, cytology and organization*. Springer-Verlag.

Peichl, L., & Wässle, H. (1981). Morphological identification of on- and off-centre brisk transient (Y) cells in the cat retina. *Proceedings of the Royal Society of London B*, *212*, 139–156.

Peters, A., Palay, S. L., & Webster, H. (1991). *The fine structure of the nervous system. Neurons and their supporting cells* (3rd ed.). Oxford University Press.

Peters, A., Proskauer, C. C., & Kaiserman-Abramof, I. R. (1968). The small pyramidal neuron of the rat cerebral cortex: The axon hillock and initial segment. *Journal of Cell Biology*, *39*, 604–619.

Pourcho, R. G., & Goebel, D. J. (1985). A combined Golgi and autoradiographic study of ($^3$H)glycine-accumulating amacrine cells in the cat retina. *Journal of Comparative Neurology*, *233*, 473–480.

Puthussery, T., Venkataramani, S., Gayet-Primo, J., Smith, R. G., & Taylor, W. R. (2013). $Na_v1.1$ channels in axon initial segments of bipolar cells augment input to magnocellular visual pathways in the primate retina. *Journal of Neuroscience*, *33*, 16045–16059.

Shepherd, G. M. (1991). *Foundations of the neuron doctrine*. Oxford University Press.

Somogyi, P. (1977). A specific "axo-axonal" interneuron in the visual cortex of the rat. *Brain Research*, *136*, 345–350.

Somogyi, P., & Hámori, J. (1976). A quantitative electron microscopic study of the Purkinje cell axon initial segment. *Neuroscience*, *1*, 361–365.

Srinivasan, Y., Elmer, L., Davis, J., Bennett, V., & Angelides, K. (1988). Ankyrin and spectrin associate with voltage-dependent sodium channels in brain. *Nature*, *333*, 177–180.

Stafford, D. K., & Dacey, D. M. (1997). Physiology of the A1 amacrine: A spiking, axon-bearing interneuron of the macaque monkey retina. *Visual Neuroscience*, *14*, 507–522.

Strettoi, E., Raviola, E., & Dacheux, R. F. (1992). Synaptic connections of the narrow-field, bistratified rod amacrine cell (AII) in the rabbit retina. *Journal of Comparative Neurology*, *325*, 152–168.

Tian, M., Jarsky, T., Murphy, G. J., Rieke, F., & Singer, J. H. (2010). Voltage-gated Na channels in AII amacrine cells accelerate scotopic light responses mediated by the rod bipolar cell pathway. *Journal of Neuroscience*, *30*, 4650–4659.

Trenholm, S., Borowska, J., Zhang, J., Hoggarth, A., Johnson, K., Barnes, S., Lewis, T. J., & Awatramani, G. B. (2012). Intrinsic oscillatory activity arising within the electrically coupled AII amacrine - ON cone bipolar cell network is driven by voltage-gated $Na^+$ channels. *Journal of Physiology*, *590*, 2501–2517.

Tsukamoto, Y., & Omi, N. (2013). Functional allocation of synaptic contacts in microcircuits from rods via rod bipolar to AII amacrine cells in the mouse retina. *Journal of Comparative Neurology*, *521*, 3541–3555.

van Wart, A., Boiko, T., Trimmer, J. S., & Matthews, G. (2005). Novel clustering of sodium channel $Na_v1.1$ with ankyrin-G and neurofascin at discrete sites in the inner plexiform layer of the retina. *Molecular and Cellular Neuroscience*, *28*, 661–673.

Vaney, D. I. (1985). The morphology and topographic distribution of AII amacrine cells in the cat retina. *Proceedings of the Royal Society of London B*, *224*, 475–488.

Vaney, D. I., Peichl, L., & Boycott, B. B. (1988). Neurofibrillar long-range amacrine cells in mammalian retina. *Proceedings of the Royal Society of London B*, *235*, 203–219.

Veruki, M. L., & Hartveit, E. (2002a). AII (rod) amacrine cells form a network of electrically coupled interneurons in the mammalian retina. *Neuron*, *33*, 935–946.

Veruki, M. L., & Hartveit, E. (2002b). Electrical synapses mediate signal transmission in the rod pathway of the mammalian retina. *Journal of Neuroscience*, *22*, 10558–10566.

Veruki, M. L., Oltedal, L., & Hartveit, E. (2010). Electrical coupling and passive membrane properties of AII amacrine cells. *Journal of Neurophysiology*, *103*, 1456–1466.

Vielma, A. H., & Schmachtenberg, O. (2016). Electrophysiological fingerprints of OFF bipolar cells in rat retina. *Scientific Reports*, *6*, 30259. https://doi.org/10.1038/srep30259

Völgyi, B., Xin, D., Amarillo, Y., & Bloomfield, S. A. (2001). Morphology and physiology of the polyaxonal amacrine cells in the rabbit retina. *Journal of Comparative Neurology*, *440*, 109–125.

Wässle, H., Grünert, U., & Röhrenbeck, J. (1993). Immunocytochemical staining of AII-amacrine cells in the rat retina with antibodies against parvalbumin. *Journal of Comparative Neurology*, *332*, 407–420.

Wässle, H., Peichl, L., & Boycott, B. B. (1981). Dendritic territories of cat retinal ganglion cells. *Nature*, *292*, 344–345.

Wässle, H., & Riemann, H. J. (1978). The mosaic of nerve cells in the mammalian retina. *Proceedings of the Royal Society of London B*, *200*, 441–461.

Westrum, L. E. (1966). Synaptic contacts on axons in the cerebral cortex. *Nature*, *210*, 1289–1290.

Wu, C., Ivanova, E., Cui, J., Lu, Q., & Pan, Z.-H. (2011). Action potential generation at an axon initial segment-like process in the axonless retinal AII amacrine cell. *Journal of Neuroscience*, *31*, 14654–14659.

Zandt, B.-J., Liu, J. H., Veruki, M. L., & Hartveit, E. (2017). AII amacrine cells: Quantitative reconstruction and morphometric analysis of electrophysiologically identified cells in live rat retinal slices imaged with multi-photon excitation microscopy. *Brain Structure and Function*, *222*, 151–182.